

Nano- and micro-characterisation on the heterogeneity of ITZs in recycled lump concrete

Hanbing Zhao^a, Yixiang Gan^b, Fulin Qu^a, Zhuo Tang^c, Shuhua Peng^d, Yangqiao Chen^a, Wengui Li^{a,*}

^a Centre for Infrastructure Engineering and Safety, School of Civil and Environmental Engineering, The University of New South Wales, NSW, 2052, Australia

^b School of Civil Engineering, The University of Sydney, NSW, 2006, Australia

^c School of Civil Engineering, Central South University, Changsha, 410075, Hunan, China

^d School of Mechanical and Manufacturing Engineering, The University of New South Wales, NSW, 2052, Australia

ARTICLE INFO

Keywords:

Recycled lump concrete
Recycled sand/recycled powder blends
Interfacial transition zone
Heterogeneity
Microscopic characterization

ABSTRACT

Recycled lump concrete (RLC) is a new sustainable construction material for filling large-sized demolished concrete lump (DCL) piles with fresh mortar or concrete. Due to the differences from conventional concrete casting technology, the heterogeneity and cohesion performance of the interfacial transition zones (ITZs) require further investigation. In this study, two types of self-compacting mortar (SCPM) were designed using blends of cement, recycled sand/recycled powder (RS/RP), and fly ash as raw materials. The filling performance of the SCPM was evaluated based on the microstructure, micromechanical properties and phase distribution within the ITZs and the adjacent matrix surrounding DCLs. Both types of SCPM effectively fill the gaps between DCLs, observed in the appearance of specimens. However, the bonding strength of bottom and oblique bottom ITZs of RLC prepared by SCPM without fly ash and superplasticizer was poor, making it impossible to produce ITZ samples from these two locations successfully. The heterogeneity and cohesion strength of the ITZs surrounding the DCLs depends on the distribution of pores and grains. Grains, including RP and fly ash, accumulated at the top and oblique top sides of the DCL due to sedimentation. Fly ash and RP effectively promoted the healing of micro-pores and cracks around DCLs but had a limited effect on pores and cracks with an average equivalent diameter greater than 1 μm. In summary, the ITZs at the top and oblique top sides of the DCLs had a denser microstructure and better bonding performance than those at other locations around the DCLs.

1. Introduction

Concrete is the most widely used construction material but comes with a high carbon footprint. The production and transportation of cement, sand and aggregate trigger a large amount of carbon emission. Recycled lump concrete (RLC) is a new type of sustainable concrete material with large-sized demolished concrete lump (DCL) piles as the skeleton and fresh concrete/mortar to fill in the gaps between the DCLs. The production of DCLs simplifies the crushing and sieving process of traditional recycled aggregate, therefore reducing the dust pollution to the air. Most importantly, DCLs can occupy most of the volume of the material, thus reducing the consumption of cement. Yan and Wu [1] reported that using large-sized DCLs as the concrete skeleton reduced cement consumption by 25 %–30 % compared with traditional recycled

aggregate concrete (RAC). Jian et al. [2] analysed the environmental impacts of RLC through life cycle assessment and found that concrete containing 30 % DCLs had a more than 30 % decrease in cumulated energy demand, eutrophication potential, and acidification potential compared with ordinary RAC. Therefore, scholars are strongly promoting the application of RLC in construction projects because of its attractive financial and environmental benefits [3,4].

For RLC, traditional concrete preparation methods are no longer suitable. Referring to the casting process of rock-filled concrete (RFC), DCLs were initially put into moulds, followed by filling the voids between the DCLs with high-fluidity fresh concrete [5]. This technique is extremely suitable for massive concrete structure constructions, because it avoids vibration and large-volume steel grid reinforcements [6]. An et al. [7] reported that this casting technique has been successfully

* Corresponding author. Centre for Infrastructure Engineering and Safety, School of Civil and Environmental Engineering, The University of New South Wales, NSW, 2052, Australia.

E-mail address: wengui.li@unsw.edu.au (W. Li).

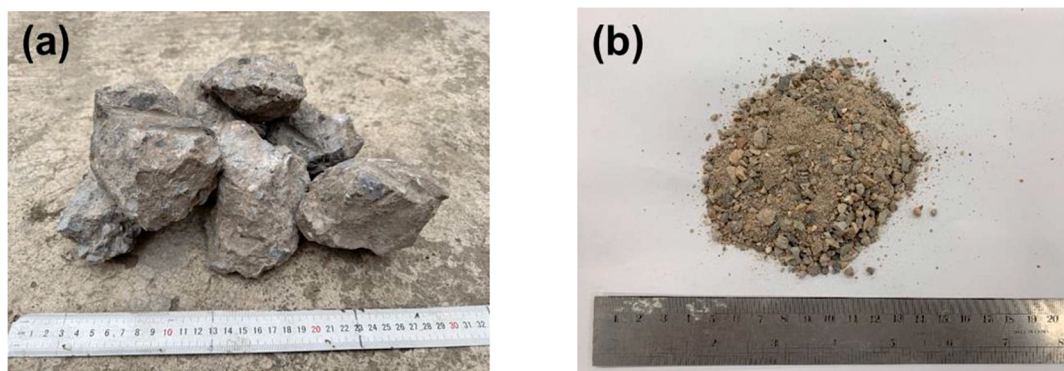


Fig. 1. DCL and RS/RP blends.

Table 1

Mixture proportion of source concrete (kg/m^3).

Cement	Coarse aggregate	Fine aggregate	Water	Water/cement ratio	Sand ratio
481	700	507	217	0.45	0.42

applied on more than 60 hydraulic engineering projects in China, and the application of RFC has exceeded 800,000 m^3 . However, the main component of DCL surface is old cement mortar. Therefore, its hardness, permeability and bonding performance with new fresh concrete are different from natural rocks [8]. Wu et al. [9–11] conducted long-term research on the mechanical properties and durability of RLC. They produced DCLs by crushing concrete structures with an original 150 mm cubic compressive strength of 47.3 MPa, and then successfully fabricated RLC specimens with a 28-day compressive strength of 38 MPa, which satisfies the compressive strength requirement of C30 concrete, although the porosity and harmful pores increased remarkably around DCLs [1,3]. Paradoxically, Lin and Wu [12] concluded in another experiment that DCLs would not cause significant changes in the pore structure of fresh concrete surrounding DCLs. The impermeability of RLC is mainly affected by the density of source concrete. Wu et al. [4] indicated that the supporting effect of DCL for concrete matrix can effectively reduce autogenous and drying shrinkage compared to ordinary RAC. However, they failed to provide a more profound explanation of the volumetric stability mechanism by observing the micromorphology of the DCL-fresh concrete interface.

The narrow region of cement paste bonded to aggregate, that is, the interfacial transition zone (ITZ), is considered to determine the mechanical properties, resistance to ion penetration, and volumetric stability of concrete [13,14]. DCL is an entirety composed of a large amount of natural aggregate and old mortar, and its physical properties are similar to ordinary recycled coarse aggregate (RCA) [4]. However, due to differences in casting procedures, it is inappropriate to transfer the test results and conclusions of ITZs in ordinary RAC to RLC. For example, RCA used to require a saturated surface drying state or a water compensation method to alleviate the impact of high water absorption of RCA [15]. For DCL, due to the excessively large size, it is difficult to eliminate the impact of the high-water absorption of the old mortar on the effective water-cement ratio within the RLC through the above methods. This leads to the difference between the bleeding phenomenon of DCL and ordinary RCA during the curing process. In addition, some scholars proposed that highly inhomogeneous ITZs may induce stress concentration under loading and cause an instant collapse of concrete structures [16]. The special casting process and large-sized aggregate of RLC make this inhomogeneity even more worthy of attention. Xie et al. [17,18] used image analysis and nanoindentation techniques to study the pore distribution and micromechanical properties of ITZ in RFC with different aggregate sizes, concrete fluidity and aggregate moisture, but

ignored the interference of rock surface inhomogeneity on the statistical results. Luo et al. [19] manufactured a modelled aggregate geopolymer concrete and found that the micromechanical properties of ITZs at the top and bottom boundaries were higher than the ITZs at lateral boundaries. However, modelled aggregate idealised the real aggregate condition.

Up to now, most research focused on the macroscopic mechanical properties and durability of RLC specimens [3,8]. The quantitative analysis of the bonding performance and heterogeneity of ITZs surrounding a DCL is insufficient. In this study, we used Portland cement, fly ash, superplasticiser and recycled sand/recycled powder (RS/RP) blends to prepare two types of fresh mortar with self-compacting capabilities to compare filling performance. Backscattered electron (BSE)-based image analysis, nanoindentation and electron dispersive spectroscopy (EDS) hypermap quantitative analysis techniques were used in this research. The bonding performance of mortar to DCLs and the heterogeneity at different positions around DCLs were comprehensively discussed through the pore structure, micromechanical properties and element distribution within ITZs and adjacent matrix. The research results are contributed to explain the mechanical performance and the degradation mechanism of RLC in hydraulic engineering structures during long-term service [20–22].

2. Experimental programme

2.1. Raw materials

In this study, DCLs (see Fig. 1 (a)) come from a batch of $\Phi 100 \times 200$ mm NAC cylinders at the age of more than one year, and the mixture proportion is shown in Table 1. The 28-day compressive strength of these cylinder specimens was approximately 41 ± 3.5 MPa. The concrete cylinders were simply crushed to obtain DCLs with a diameter of approximately 80–100 mm. The RS/RP blends with a diameter below 4.75 mm, as shown in Fig. 1 (b) generated during the crushing process were collected and used to prepare self-compacting mortar (SCPM). Three groups of RS/RP blends with a mass of 1 kg each were used to test particle size distribution, and the results are shown in Table 2. According to ASTM C29-17 (Standard Test Method for Bulk Density ("Unit Weight") and Voids in Aggregate) and ASTM C128-22 (Standard Test Method for Relative Density (Specific Gravity) and Absorption of Fine Aggregate), the pore ratio, relative density and water absorption ratio of the RS/RP blends were 0.226, $2320.72 \text{ kg}/\text{m}^3$ and 6.38 %, respectively. General purpose Portland cement, fly ash and recycled powder were the main binder materials in SCPM. The chemical composition of binder materials tested by X-ray fluorescence (XRF) is shown in Table 3. Tap water and naphthalene-based superplasticizer (SP) were used to blend constituents.

Table 2

Proportions of different size particles in RS/RP blends.

2.36–4.75 mm	1.18–2.36 mm	0.6–1.18 mm	0.3–0.6 mm	0.15–0.3 mm	0–0.15 mm
46.8 ± 3.5 %	16.6 ± 1.3 %	11.4 ± 0.5 %	10.4 ± 0.9 %	2.1 ± 0.2 %	12.6 ± 1.1 %

Table 3

Chemical composition of powder materials (wt.%).

Oxide	Na ₂ O	MgO	Al ₂ O ₃	SiO ₂	P ₂ O ₅	SO ₃	K ₂ O	CaO	TiO ₂	V ₂ O ₅	Mn ₃ O ₄	Fe ₂ O ₃	ZnO	LOI
Cement	0.21	1.41	5.01	18.46	0.19	2.44	0.45	62.49	0.30	0.02	0.18	2.91	0.02	5.91
Fly ash	0.57	0.57	27.45	61.34	0.22	0.04	1.30	1.91	1.05	0.01	0.03	2.85	<0.01	2.65
RP	1.09	1.51	10.13	57.82	0.15	0.49	1.29	12.61	0.66	0.01	0.08	4.46	0.02	9.68

Table 4

Mixture proportion of self-compacting mortar (SCPM).

Mix ID.	Raw materials (kg/m ³)						Flow diameter (mm)
	Cement	Water	Additional water	RS/RP	Fly ash	SP	
SCPM-1	450	225	57	900	0	0	201
SCPM-2	337.5	180	57	900	112.5	1	231

2.2. Mixture design and specimen preparation

Approximately 3–4 DCLs were placed into a 200 mm × 200 mm cubic mould, and the spaces between the DCLs were subsequently filled by SCPM. In this study, two mortar mixture with high flowability were designed, labelled SCPM-1 and SCPM-2, respectively, as shown in Table 4. The main ingredients of the first mortar mixture were based on cement and RS/RP. To ensure high fluidity and avoid mortar delamination, the water-cement ratio was finally determined to be 0.5 after repeated attempts. 57 kg/m³ of additional water was used to compensate for the water absorbed by RS/RP during mixing process. The water-cement ratio of the second mortar was determined to be 0.4. Fly ash and SP were used to improve the flowability of the mortar. Here we focus on the fluidity difference between the two mixture proportions. The effects of water-cement ratio, fly ash and superplasticizer on mortar performance are well known and therefore will not interfere with the analysis of subsequent test results. In the SCPM preparation process, cementitious materials and RS/RP were dry-mixed for 2 min. For SCPM-2, water with SP solution was added to the bowl slowly and mixed thoroughly for another 4 min. Mini-slump tests were conducted to determine the flowability of the two SCPM according to ASTM C1437 (Standard Test Method for Flow of Hydraulic Cement Mortar). A conical mould with top opening and bottom opening diameters of 70 mm and 100 mm, respectively was filled with mortar. Due to the high flowability of the mortar in this study, after carefully lifting away the mould, the table was

dropped 10 times in 15 s rather than 25 times required in ASTM C1437 [23]. Otherwise, the flow diameter of SCPM would exceed the measuring range. The flow diameter of SCPM-1 and SCPM-2 is shown in Table 4, which satisfies the requirements of self-compacting mortar [24].

The prepped SCPM was smoothly poured into the mould without vibration as shown in Fig. 2. The specimens were then covered with a layer of plastic film and cured in the moulds for 24 h before being transferred to a standard curing room (23 ± 3 °C, 95 % RH) for 28 d. Cubic specimens with a side length of 200 mm were used for compressive strength tests at a loading speed of 0.4 MPa/s according to GB/T 50081 (Standard for test method of mechanical properties on ordinary concrete). Each group of tests were repeated three times.

Another group of 100 mm × 100 mm cubic specimens with a single DCL was fabricated using SCPM-1 and SCPM-2 in the same procedure, and then the specimens were cut along the cross-section where the maximum diameter of DCL was located to minimize the error in the evaluation of the microscopic properties of ITZs [25]. As shown in Fig. 3, five regions from the top side to the bottom side of the DCL were used to statistically analyse the heterogeneity of the ITZ within the RLC prepared by SCPM-2. The sample at the corresponding regions are labelled as SCPM-2-1, SCPM-2-2, SCPM-2-3, SCPM-2-4 and SCPM-2-5, respectively. Due to poor bonding strength of SCPM-1 at bottom and oblique bottom side of DCL, only SCPM-1-1, SCPM-1-2 and SCPM-1-3 (#1, #2 and #3 regions respectively in Fig. 3) were obtained for RLC prepared by SCPM-1. Concrete fragments containing ITZs were impregnated with epoxy resin and cured in the room temperature for one day. Referring to the previous procedure [19,26,27], the samples were ground with 240, 600 and 1200 grit abrasive paper for 10 min in sequence. The sample surface was then polished by 9 µm, 3 µm, 1 µm and 0.05 µm diamond solution for 15 min in sequence. After each polishing, the samples were put in an ultrasonic bath for 2 min to remove residual particles on the sample surface. Finally, the samples were placed in a vacuum drying oven and dried at 60 °C for 48 h.

**Fig. 2.** Fabrication process of RLC specimens.

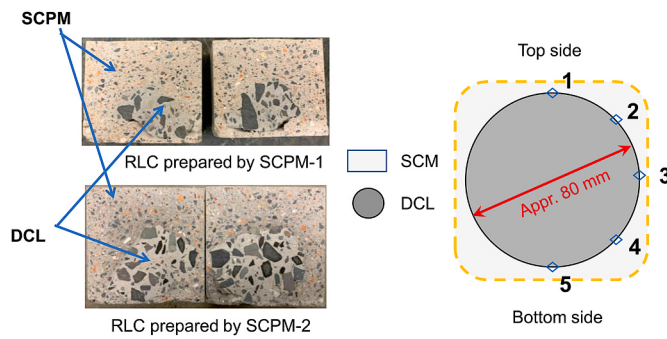


Fig. 3. Location distribution of samples for microscopic tests.

2.3. Nanoindentation tests

Nanoindentation is an important technique for detecting the micro-mechanical properties of cementitious materials. It can be used to evaluate the cohesion performance of cement paste bonded to DCLs at different locations. A nanoindenter equipped with Berkovich tip was used for grid nanoindentation tests. The layout of testing points is shown in Fig. 4. To avoid overlapping to testing points, the horizontal and vertical spacing between the testing points were 5 μm and 10 μm , respectively [28]. Each grid nanoindentation region contains 20 \times 5 testing points from DCL to SCPM matrix. The test regions close to sands and large pores were artificially avoided. Two groups of such grid nanoindentation tests were performed at the interface between SCPM and DCL at each location designed in Fig. 3. Indentation depth was controlled by peak force, which was set to 1200 μN in this study [29]. When the indentation force reached 1200 μN , the tip was maintained at the peak force for 5 s and then unloaded to 10 % of the peak force and maintained for another 2 s. The elastic modulus and hardness of cement paste can be calculated by Eqs. (1)–(3) based on indentation load (P), peak load (P_{\max}), indentation depth (h), project contact area (A), reduced elastic modulus (E_r), characteristics of the tip (elastic modulus, $E_i = 1140 \text{ GPa}$ and Poisson's ratio, $\nu_i = 0.07$) and characteristics of cement paste (Poisson's ratio, $\nu = 0.2$) [30].

$$\frac{1}{E_r} = \frac{1 - \nu^2}{E} + \frac{1 - \nu_i^2}{E_i} \quad (1)$$

$$S = \frac{dP}{dh} \Big|_{h=h_{\max}} = \frac{2}{\sqrt{\pi}} E_r \sqrt{A} \quad (2)$$

$$H = \frac{P_{\max}}{A} \quad (3)$$

2.4. BSE-based image analysis

Samples were sputter-coated with a layer of 10 nm carbon before the tests since concrete is an insulating material. At least 30 backscattered electron (BSE) images at a magnification of 500 \times were taken for #1 to #5 locations as shown in Fig. 5(a)–(h). Due to the extremely poor bonding performance of SCPM-1-4 and SCPM-1-5 (see Fig. 3), the samples could not withstand the force from the clamp and blade during

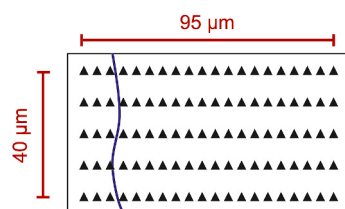


Fig. 4. Schematic diagram of grid nanoindentation tests.

the cutting process. Therefore, only 8 samples were prepared in this study (3 samples for SCPM-1 and 5 samples for SCPM-2). According to the grey gradient theory proposed by Wong et al., [31] constituents within cement paste can be easily captured and segmented. This technique has been successfully used in previous studies [26,27,32]. Taking Fig. 5 (h) as an example, the segmented image is shown in Fig. 5 (i). The black area represents pores and cracks; the yellow area represents hydration products; the blue area represents unreacted particles, including clinkers and fly ash; and the green area represents DCL. It should be noted that the pores on the fly ash and holes left by fly ash spalling were regarded as part of the clinkers rather than pores or hydration products in the cement paste [19]. Subsequently, the BSE images were divided into 20 continuous strips with a width of 5 μm from the DCL surface to the SCPM matrix. The proportions of hydration products, clinkers and fly ash were used to identify ITZ width. The equivalent diameter distribution of pores and cracks was calculated and used to evaluate the performance of ITZs at different locations.

2.5. BSE-EDS hypermap analysis

Different from traditional electron dispersive spectroscopy (EDS) mapping analysis, EDS hypermap can display element distribution on BSE images as well as provide quantitative results [33]. This contributed to obtaining a deeper understanding of the SCPM chemical composition based on Al/Ca and Si/Ca at different regions near the DCL surface. To ensure that sufficient data were available for quantitative analysis, the accelerating voltage was set as 15 kV and the deadtime was kept at around 30 % [33]. In a rectangular area of 50 $\mu\text{m} \times 34 \mu\text{m}$, the resolution was set to 1024 \times 768 pixels with 256 s dwell time per pixel [33]. As a result, the acquisition time of each hypermap was around 1 h. Subsequently, the spectrum signal of Al, Si, Ca, Na, K etc. based on hypermaps were quantified by the Aztec built-in QuantMap function and saved as txt files.

The framework, edxia, which is coded in python and included as a plugin to Glue software was used to process the quantised txt files. Due to the limitations of the EDS detector and scanning period, the hypermap usually needs to experience a denoising process to eliminate densely dotted textures on the elemental maps. After repeated attempts, the total variation algorithm with the weight of 0.1 can achieve the most ideal denoising results. Therefore, it was used to process elemental maps in this research. The EDS spectrum of each pixel in Hypermaps was presented as data points in Si/Ca vs. Al/Ca figures. Based on previous experience [34], the hydration degree and phase composition of SCPM bonded to the DCL surface at different locations can be obtained through quantified data.

3. Results and analysis

3.1. Compressive strength and failure face

The 7-day and 28-day compressive strength of RLC specimens are shown in Fig. 6. The compressive strengths of RLC prepared with SCPM-1 and SCPM-2 were 28.10 MPa and 30.05 MPa, respectively at 7 days. When the curing period reached 28 days, the compressive strength of both groups of RLC can exceed 33 MPa. Considering the size effect on the test results, the RLC fabricated in this study can be applied to roads, hydraulic structures and some non-critical regions [7,35]. Among them, the compressive strength of RLC made with SCPM-2 was slightly higher than that of its counterpart due to the lower water-cement ratio. In addition, compared with the 7-day compressive strength, the difference in compressive strength between the two groups of specimens was reduced to only 1.38 MPa on the 28th day. The failure patterns in Fig. 6 show that DCL was mainly through-break, while the DCLs near the middle of the pressure surface was relatively intact because friction limited the displacement of top and bottom ends.

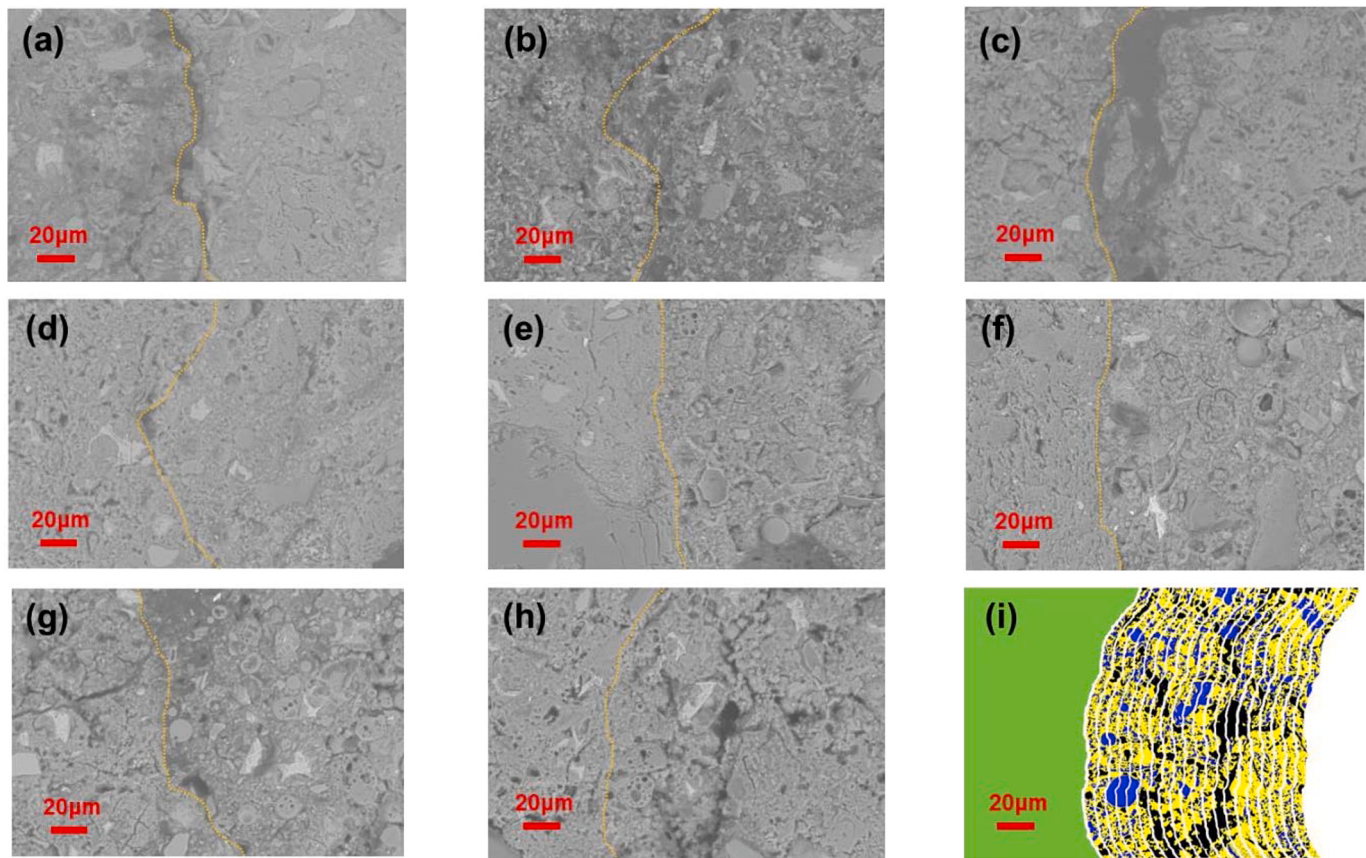


Fig. 5. BSE images and image analysis at DCL-cement paste interfaces: (a) SCPM-1-1; (b) SCPM-1-2; (c) SCPM-1-3; (d) SCPM-2-1; (e) SCPM-2-2; (f) SCPM-2-3; (g) SCPM-2-4; (h) SCPM-2-5; (i) Constituents segmentation.

Note: the number after SCPM-1 and SCPM-2 represents a corresponding location in Fig. 3. The same as below.

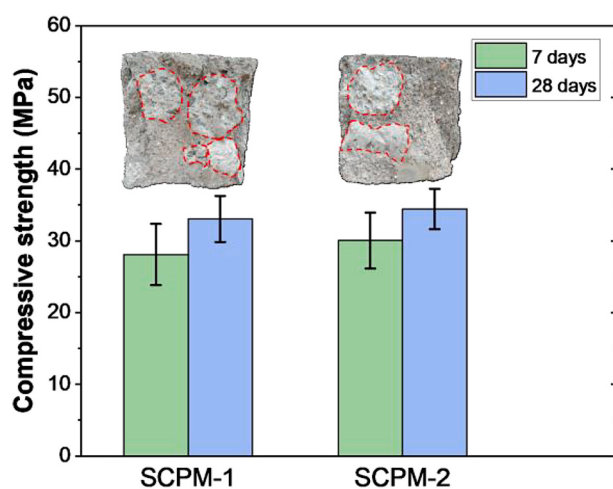


Fig. 6. Compressive strength test results of RLC.

3.2. ITZ width identification

The BSE-based image analysis technique was used to segment the cement paste into pores and cracks, hydration products, and unreacted particles according to grey thresholds. Statistical analysis of the successive strips with 5 μm in width divided in Section 2.4 can reveal the variation trend of the constituent proportions from the DCL surface to the SCPM matrix. Since the bonding strength of the cement paste at the SCPM-1-4 and SCPM-1-5 is extremely poor and qualified samples cannot

be successfully produced, the performance of the #1, #2 and #3 regions will be used to analyse heterogeneity of RLC prepared by SCPM-1. The corresponding results are shown in Fig. 7.

It can be clearly seen that the porosity of SCPM-1 on the DCL surface is significantly higher than the regions far away from the DCL. This phenomenon is common even in ordinary RAC [36]. The calcium silicate hydrate (C-S-H) gel with cohesion properties was created in the hydration reaction of cementitious materials, which makes the paste matrix attach to the aggregate [37]. Therefore, the aggregate-paste matrix interface is the region with a high probability of gaps. This is more significant in RLC. For example, Jan and Wu [3] found a higher content of pores, cracks and crystals at ITZs of RLC because DCLs did not fully mixed with fresh concrete and form a poor bonding. The image analysis results show that the volume fraction of pores and cracks of SCPM-1-1 and SCPM-1-2 at 2.5 μm from the DCL surface reached more than 0.2, whereas these data in the paste matrix 60 μm away from the DCL surface dropped rapidly to around 0.08–0.12. This proves that SCPM is more likely to form a dense microstructure in the matrix area. In contrast, the proportion of pores and cracks of SCPM-1-3 on the DCL surface was more than twice that of the first two locations. Previous studies have also confirmed that the porosity of cement paste is usually higher on the lateral face of aggregate [19]. RCL amplifies this phenomenon because the filling effect of SCPM is extremely dependent on the shear stress generated by gravity vs. the yield stress of the fresh mortar. According to Bingham fluid theory, when the shear stress of SCPM is higher than the yield stress, the mortar can exhibit liquid performance [38]. Due to the narrow channel between the mould sidewall and the lateral side of the DCL, the shear stress generated by the gravity of SCPM could be very low and cannot overcome the yield stress. Only cement paste with extremely low yield stress could pass through. Thus, the proportion of pores and

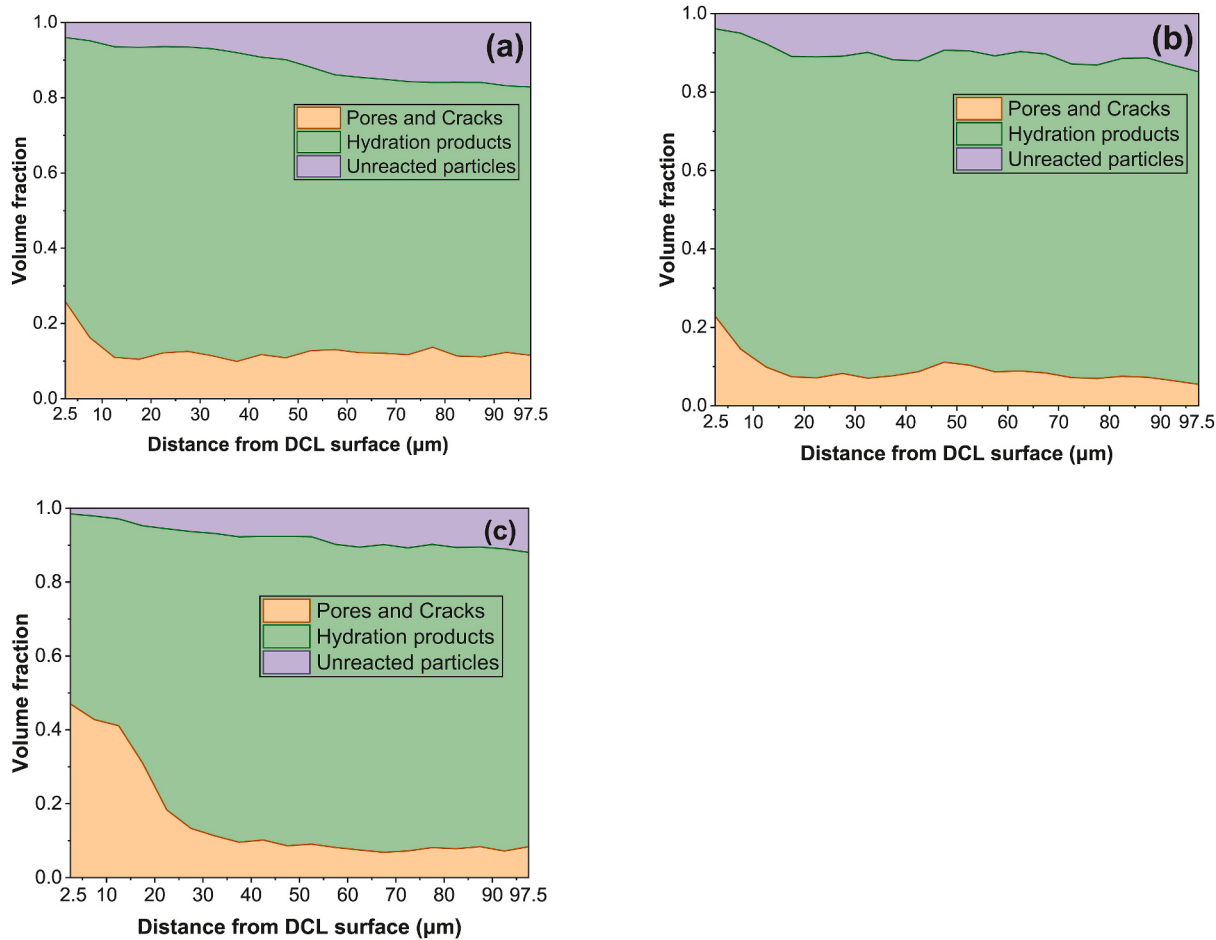


Fig. 7. Constituent distribution from DCL surface to SCPM-1 matrix: (a) SCPM-1-1; (b) SCPM-1-2; (c) SCPM-1-3.

cracks at the lateral side was over the limit. The proportion of pores and cracks of SCPM-1-3 in the area far from the DCL surface was maintained at about 0.09, which was close to that in the corresponding areas of SCPM-1-1 and SCPM-1-2.

Although the old mortar of DCLs makes its surface loose and porous, which is different from natural rock, the stiffness of DCLs is still obviously higher than that of fresh SCPM because of long-term curing. This means that there is also an obvious wall effect in RLC. The volume fraction of hydration products and unreacted particles gradually increased from the DCL surface to the SCPM matrix and maintained a stable value. The volume fraction of unreacted particles at SCPM-1-1 and SCPM-1-2 was slightly higher than that at SCPM-1-3 because most clinkers and particles accumulated on the top and oblique top sides of DCL due to sedimentation. In addition, the content of hydration products of SCPM-1-3 near the DCL surface was lower than that of SCPM-1-1 and SCPM-1-2 because of the excessively high porosity of SCPM-1-3. In summary, it can be estimated that SCPM-1-3 is the weakest site among the three detected regions in RLC prepared by SCPM-1.

The image analysis results of SCPM-2 are shown in Fig. 8. The porosity of cement paste near the DCL surface was significantly higher than that of the paste matrix in SCPM-2-1 and SCPM-2-4, but this phenomenon did not appear in SCPM-2-2, SCPM-2-3 and SCPM-2-5. This is because superplasticizer and fly ash helped SCPM-2 achieve higher fluidity at a low water-cement ratio. In addition, 25% by mass of cement was replaced by fly ash to help evenly distribute the particles in the cement paste. The phenomenon of the excessively high proportion of pores and cracks on the DCL surface in SCPM-2-1 is probably due to the segregation and sedimentation of larger particles, which makes the C-S-H gel insufficient [39]. However, this phenomenon rapidly eased at a

distance of 20 μm from the DCL surface. For SCPM-2-4, it can be attributed to the more significant sedimentation of unreacted particles. In general, due to the limitations of the novel casting method of RLC, the porosity at the bottom of DCL was slightly higher than that at the top and lateral sides. For the diameters of pores and cracks, they will be discussed in detail in Section 3.3.

Fig. 8 shows that the distribution of hydration products and unreacted particles was relatively uniform compared to SCPM-1 in Fig. 7, which confirms the theory that fly ash contributes to the evenly distribution of particles in the cement paste. Since the pozzolanic reaction speed of fly ash is generally much lower than the hydration reaction speed of cement, there were still a large number of incompletely reacted fly ash particles in the samples during observation. As a result, the volume fraction of unreacted particles in SCPM-2 was maintained at 0.2–0.4, especially for SCPM-2-2, SCPM-2-3 and SCPM-2-5. Correspondingly, the decrease in the relative content of cement in SCPM-2 resulted in a lower proportion of hydration products in the cement paste than that in SCPM-1.

Hydration products and unreacted particles are more suitable for determining ITZ width than pores and cracks with a high degree of non-uniformity [40]. The coefficient of difference (*CoD*) for hydration products and unreacted particles will be used for identifying ITZ width. It can be calculated as [40]:

$$CoD_H = \frac{|P_{Hi} - P_{H0}|}{P_{H0}} \quad (4)$$

$$CoD_U = \frac{|P_{Ui} - P_{U0}|}{P_{U0}} \quad (5)$$

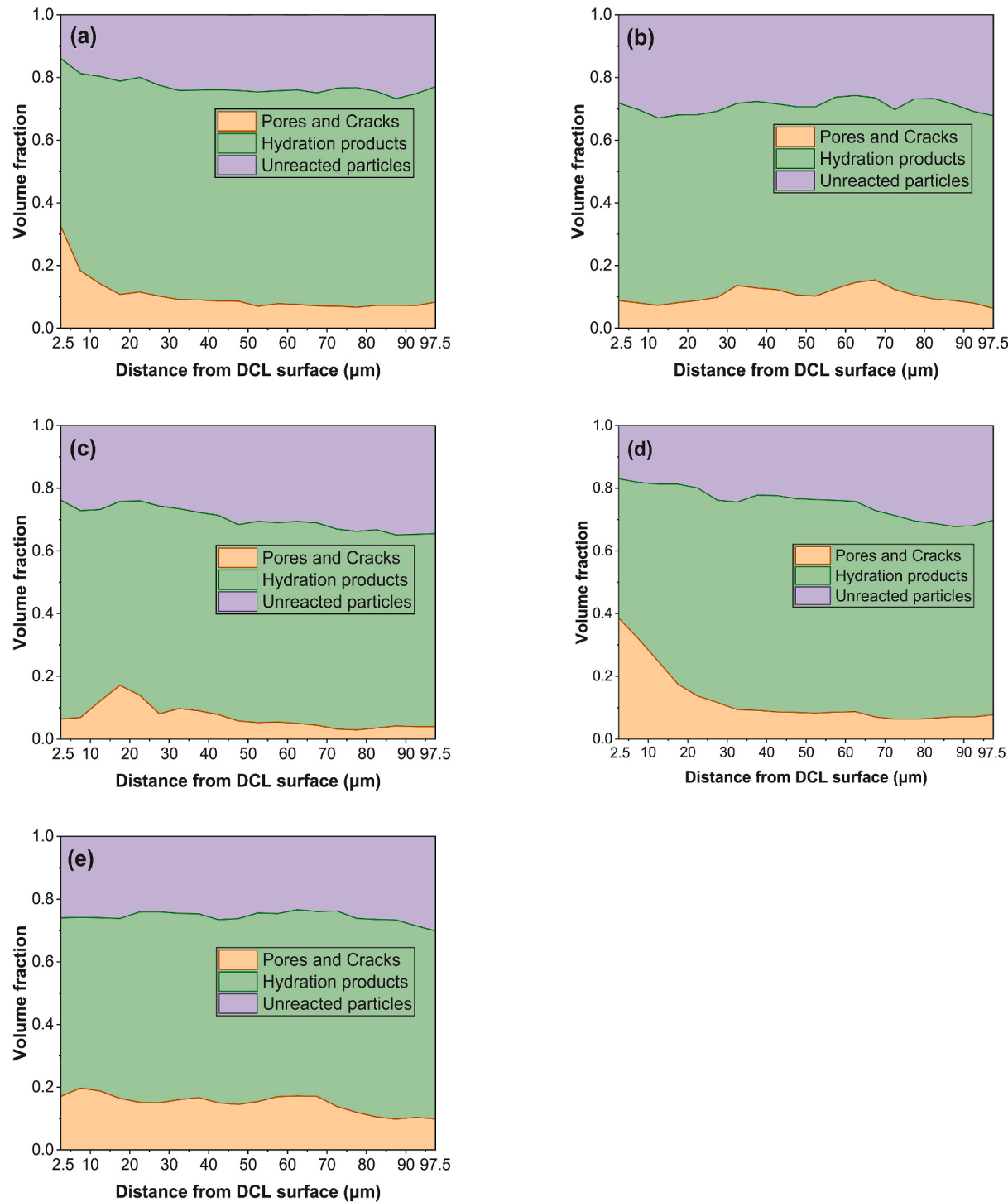


Fig. 8. Constituent distribution from DCL surface to SCPM-2 matrix: (a) SCPM-2-1; (b) SCPM-2-2; (c) SCPM-2-3; (d) SCPM-2-4; (e) SCPM-2-5.

where CoD_H and CoD_U represent the coefficient of difference of hydration products and unreacted particles, respectively. P_{Hi} and P_{Ui} represent volume fraction of hydration products and unreacted particles in the i th strip. P_{H0} and P_{U0} represent the volume fraction of hydration products and unreacted particles in the first strip, respectively.

It is generally believed that the region where CoD_H and CoD_U tend to be stable simultaneously can be treated as the paste matrix [27,40]. Accordingly, ITZ widths of SCPM-1 and SCPM-2 at different locations could be identified, as shown in Figs. 9 and 10, respectively. For SCPM-1-1, CoD_H and CoD_U remained around 0.18 and 2.98 after being

58 μm away from the DCL surface, while for SCPM-1-2, CoD_H and CoD_U fluctuated between 0.1–0.2 and 1.5–2.5, respectively, after being only 18 μm away from the DCL surface. Therefore, it can be determined that the ITZ width of SCPM-1-1 and SCPM-1-2 was 58 μm and 18 μm respectively. The volume fraction of hydration products and unreacted particles in SCPM-1-3 varied in a larger range with the distance to the DCL surface. Hydration products and unreacted particles stabilized at approximately 0.59 and 5.88 at 53 μm , respectively. Therefore, the ITZ width of SCPM-1-3 was 53 μm .

The CoD_H and CoD_U of SCPM-2 at each region were significantly lower than the corresponding values of SCPM-1 as shown in Fig. 10.

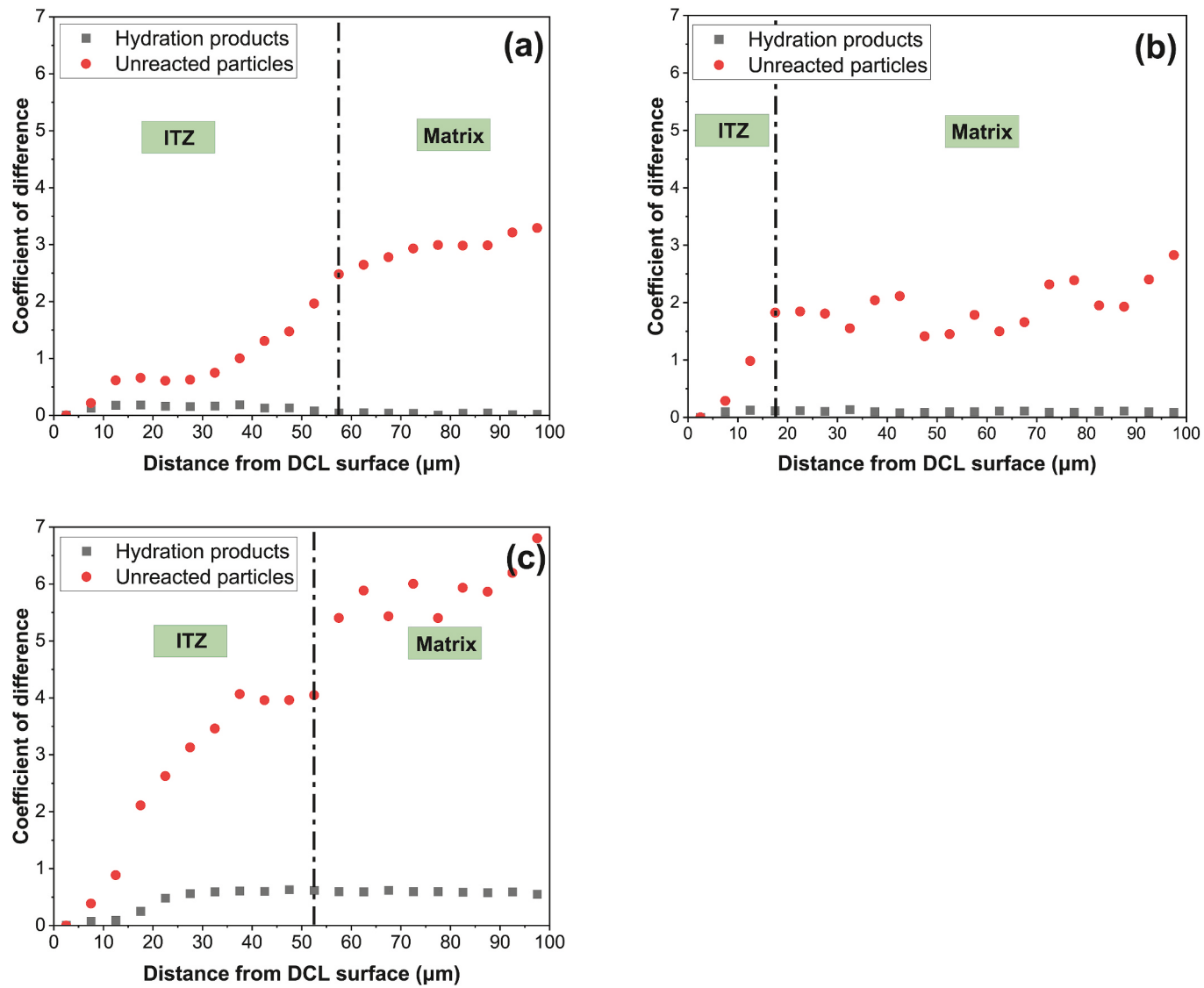


Fig. 9. ITZ width identification for SCPM-1: (a) SCPM-1-1; (b) SCPM-1-2; (c) SCPM-1-3.

Moreover, CoD_H and CoD_U of SCPM-2 were closer, and even the difference between CoD_H and CoD_U of SCPM-2-1 after stabilization at 33 μm from the DCL surface did not exceed 0.6. This demonstrated that using SCPM-2 to prepare RLC significantly alleviated the heterogeneity of ITZ and matrix in various areas near DCL surface. In a similar method, it can be confirmed that the ITZ widths of SCPM-2-1, SCPM-2-2, SCPM-2-3, SCPM-2-4 and SCPM-2-5 were 33 μm, 13 μm, 48 μm, 78 μm and 23 μm, respectively. The ITZ widths of the first three regions of SCPM-2 were narrower than those of the corresponding regions of SCPM-1. In addition, it should be acknowledged that the ITZ width of RLC is relatively high, among which the ITZ of SCPM-1-1, SCPM-1-3 and SCPM-2-4 is wider than the normal concrete ITZ with the width range of 15–50 μm [41] because of the novel casting method adopted in this research. However, ITZ width cannot be regarded as a decisive basis for determining cement paste bonding strength because it is determined by the CoD of constituents [27].

3.3. Pore and crack measurement results

The pores and cracks in the ITZ and the adjacent paste matrix within 50 μm were identified using a BSE-based image analysis technique. The average equivalent diameters were calculated based on the area of pores and cracks, and the quantity proportion distribution curves are shown in

Fig. 11. The black areas in ITZ and matrix BSE images are pores or cracks.

As can be seen from Fig. 11 (a), in the ITZ of RLC prepared by SCPM-1, the average equivalent diameter of pores and cracks was mainly concentrated in 0.2–0.3 μm, among which the ratio of pores and cracks at SCPM-1-3 in this range reached 0.62. Combined with the volume fraction of pores and cracks in the ITZ obtained in Fig. 7, it can be concluded that there were more pores and cracks in the ITZ at SCPM-1-3, although more than 60 % of the pores were small pores and cracks with an equivalent diameter of 0.2–0.3 μm. In comparison, the average equivalent diameter of pores and cracks in the ITZ of RLC prepared by SCPM-2 was more evenly distributed in a wide range. Taking SCPM-2-3 as an example, the proportions of pores and cracks with average equivalent diameters within 0.2–0.3 μm and 1–2 μm were 0.43 and 0.12, respectively, while for SCPM-1-3, the corresponding proportions were 0.62 and 0.04, respectively. This is because SCPM-2 had higher flowability and the grains such as RP and fly ash in SCPM-2 had the ability to fill small pores and cracks [42]. However, large pores and cracks cannot be effectively healed, resulting in a phenomenon in which the quantity proportion of small pores and cracks decreased, and the relative quantity proportion of large pores and cracks improved. In the comparison of ITZs attached to different locations of RLC prepared by SCPM-2, SCPM-2-5 had the highest quantity proportion of pores and cracks

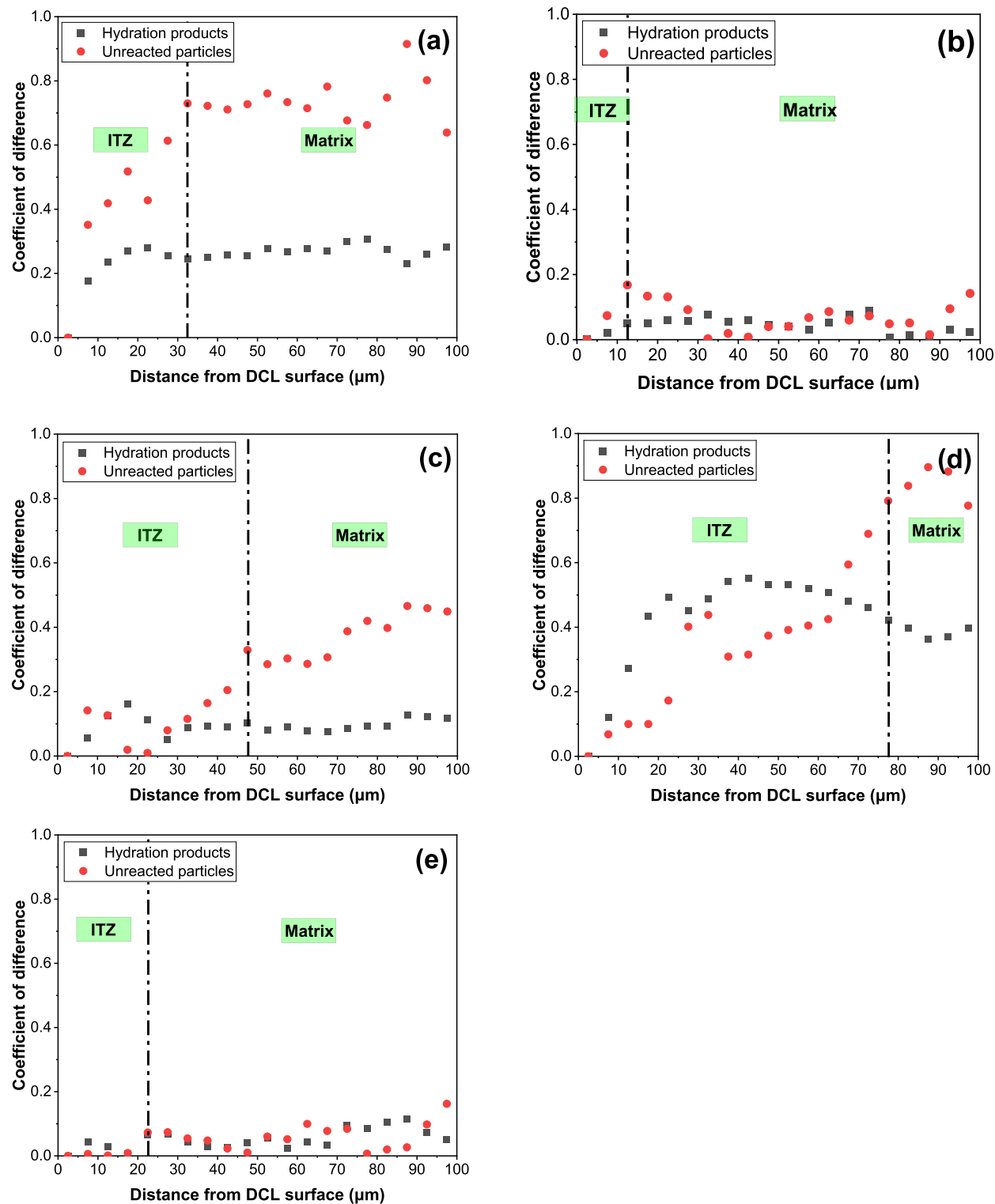


Fig. 10. ITZ width identification for SCPM-2 specimens: (a) SCPM-2-1; (b) SCPM-2-2; (c) SCPM-2-3; (d) SCPM-2-4; (e) SCPM-2-5.

with equivalent diameter between 1 and 2 μm , as shown in Fig. 11 (b), because the narrow region at the bottom side of the DCL cannot be perfectly filled by SCPM-2, resulting in an excessive number of large voids at SCPM-2-5.

The average equivalent diameter of pores and cracks within SCPM-1 matrix at each location was still concentrated in the range of 0.2–0.3 μm , but the degree was alleviated when compared with that within ITZ. As shown in Fig. 11 (c), the proportion of pores and cracks with equivalent

diameters of 0.2–0.3 μm in the matrix of SCPM-1-3 decreased to 0.51, while the relative proportion of pores and cracks with diameters of 1–2 μm increased to 0.10. This is probably due to the higher content of particles such as RP in the matrix, which helped fill the small-sized pores and cracks through physical and chemical actions [43]. Luo et al. [19] pointed out that due to the wall effect of aggregate, more particles gathered at locations far away from the aggregate especially at the lateral surface. In addition, RP possesses secondary hydration capacity,

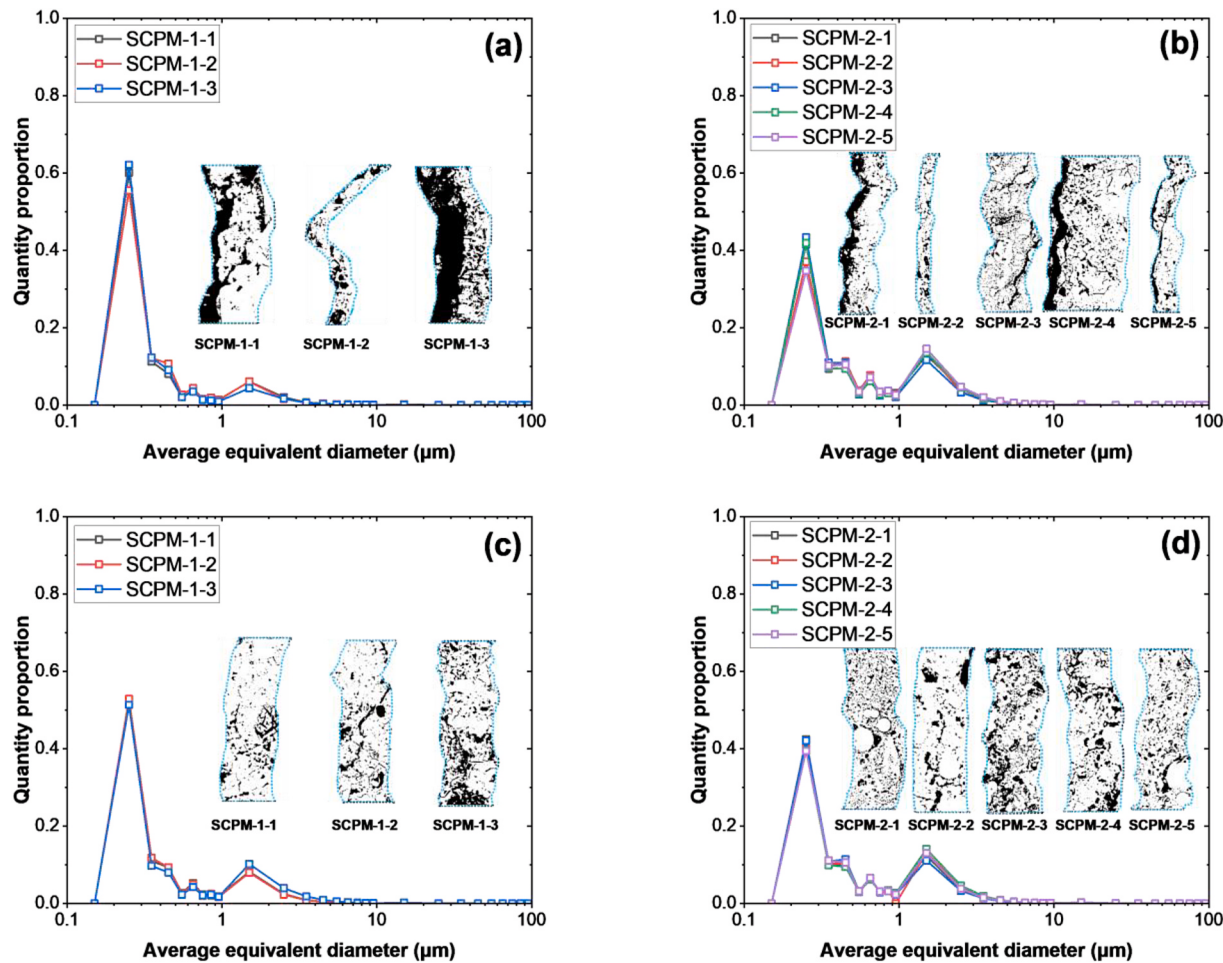


Fig. 11. Pore and crack size distribution within ITZs and matrix: (a) SCPM-1 ITZ; (b) SCPM-2 ITZ; (c) SCPM-1 matrix; (d) SCPM-2 matrix.

which can create more C-S-H gel and fill small pores [43]. A similar phenomenon also occurred in the SCPM-2 matrix, as shown in Fig. 11 (d). The average equivalent diameter distribution curves of pores and cracks within SCPM-2 matrix at each location were almost overlapping, with only slight differences at the two peaks of 0.2–0.3 μm and 1–2 μm, and the proportions remained around 0.4 and 0.13, respectively.

The average equivalent diameter data of pores and cracks within the ITZ and matrix were statistically analysed and converted into cumulative proportion curves as shown in Fig. 12. In the average equivalent diameter range of 0.25–2.5 μm, the cumulative proportion of pores and cracks of ITZ at SCPM-1-3 was higher than that of SCPM-1-1 and SCPM-1-2 as shown in Fig. 12 (a), indicating that there were more pores and cracks between 0.25 and 2.5 μm in the ITZ of SCPM-1-3. This phenomenon also occurred in the ITZ of RLC prepared by SCPM-2, as shown in Fig. 12 (b). Xie et al. [17] stated that the filling capacity of SCPM depended on the yield stress and shear stress of the cement paste. The shear stress generated by the gravity of SCPM is normally higher than the yield stress, so SCPM has better fluidity. However, for some narrow gaps between DCLs, such as the lateral side of DCLs, the shear stress cannot significantly exceed the yield stress [17]. As a result, it is difficult for SCPM-1 and SCPM-2 to pass through the narrow channel between the lateral side of the DCL and the mould to form strong bonding strength on the DCL surface. For ITZs at regions #1 and #2, the cumulative proportions of pore and crack sizes were similar, especially the cumulative proportion curves with average equivalent diameter above 0.65 μm were almost overlapped. As shown in Fig. 12 (b), the curve of SCPM-2-5 was always at the bottom in the whole range of 0.25–2.5 μm, indicating that among the five regions, the ITZ at SCPM-2-5 had the

highest proportion of large pores with an average equivalent diameter exceeding 2.5 μm.

Fig. 12 (c) shows that the cumulative proportion of pore and crack sizes in the matrix of SCPM-1-3 was lower than that of SCPM-1-1 and SCPM-1-2, which is opposite to the condition of ITZ. Similar to SCPM-2-5 in Fig. 12 (b), the matrix at SCPM-1-3 contained more large pores and cracks with equivalent diameters over 2.5 μm, and RP cannot heal these large voids effectively. In contrast, the matrix of SCPM-2 around the DCL possessed better uniformity. The cumulative proportions of pore and crack sizes in the SCPM-2 matrix were closer than ITZ cases as shown in Fig. 12 (d). The maximum cumulative proportion of SCPM-2-3 and SCPM-2-4 at 0.65 μm did not exceed 0.06.

3.4. Nanoindentation test results

The micromechanical properties of SCPM attached to the DCL surface can reflect the bonding strength of the DCL-SCPM interface. About three columns of nanoindentation testing points were designed on the DCL, and the identified ITZ and matrix regions based on the BSE-image analysis are labelled in Figs. 13–16. Fig. 13 shows the elastic modulus of SCPM-1 attached to DCLs. The elastic modulus of DCL was approximately 28.57 GPa. However, the elastic modulus of ITZ at SCPM-1-1, SCPM-1-2 and SCPM-1-3 decreased to 23.75 GPa, 22.30 GPa and 17.59 GPa, respectively. The reasons for the decrease in elastic modulus in the ITZ include higher water-cement ratio, higher porosity and shorter curing age than DCLs. For the matrix, the elastic modulus showed higher micromechanical properties, that is 24.70 GPa, 23.80 GPa and 17.83 GPa, respectively due to more unreacted particles and

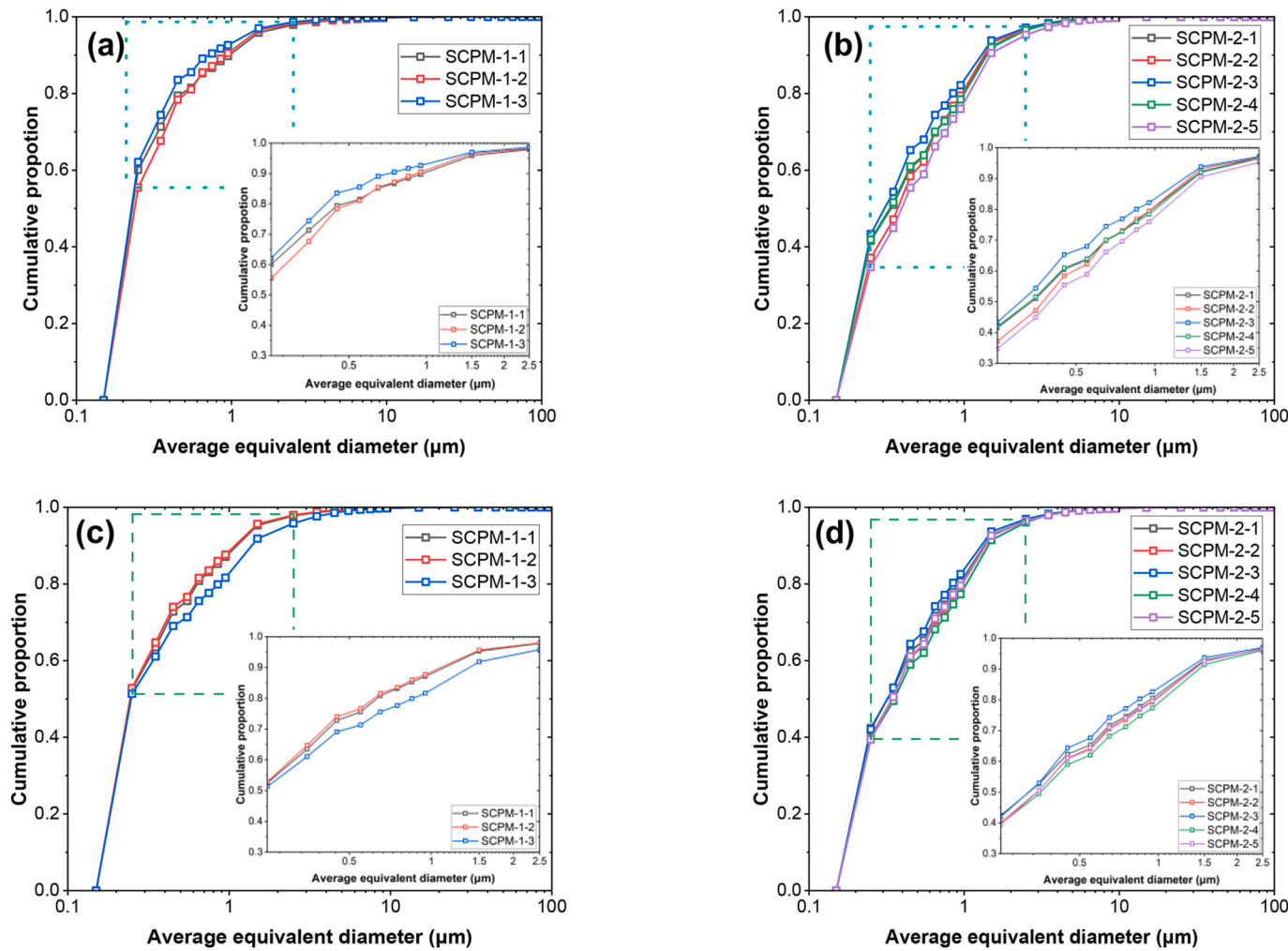


Fig. 12. Cumulative proportion distribution of pore and crack size within ITZs and matrix: (a) SCPM-1 ITZ; (b) SCPM-2 ITZ; (c) SCPM-1 matrix; (d) SCPM-2 matrix.

less pores and cracks.

The hardness of SCPM-1 around DCL showed a similar phenomenon as shown in Fig. 14. The average hardness of DCL was about 1.72 GPa. However, the hardness of ITZ at SCPM-1-1, SCPM-1-2 and SCPM-1-3 reduced to 1.12 GPa, 1.05 GPa and 1.10 GPa, respectively. For the matrix, the hardness was around 1.50 GPa, 1.45 GPa and 1.01 GPa, respectively. The variation of hardness followed the elastic modulus, but the difference between regions was not obvious compared to the elastic modulus. Some testing points even show lower elastic modulus but higher hardness. This is because cement-based materials are typically anisotropic, with differences in the elastic modulus and hardness of multi-phases leading to this phenomenon [29]. In addition, the peak force was designed to be 1200 μN to ensure sufficient test data at ITZ in this study, and the corresponding indentation depth for C-S-H was 300 nm. A shallow indentation depth may also cause deviations in the elastic modulus and hardness calculation results [27].

Due to the lower water-cement ratio and the addition of fly ash, the elastic modulus of ITZs at SCPM-2-1 and SCPM-2-2 was 29.36 GPa and 25.34 GPa, respectively (see Fig. 15), which were slightly higher than the corresponding locations of SCPM-1. However, the elastic modulus of ITZs at SCPM-2-3, SCPM-2-4 and SCPM-2-5 decreased rapidly to 18.35 GPa, 13.18 GPa and 11.94 GPa, compared to the former two locations, because SCPM-2 cannot perfectly fill lateral, bottom and oblique bottom sides of DCL. Therefore, more low-density C-S-H, pores and cracks accumulated at these locations. Due to the contribution of superplasticizer and fly ash to the uniform distribution of constituents, the average elastic modulus of matrix was slightly higher than that of

adjacent ITZ, which is consistent with the relative relationship between the elastic modulus of ITZ and paste matrix in previous studies [44,45].

Similar conclusions can be drawn from hardness, as shown in Fig. 16. The average hardness of ITZ at SCPM-2-1 and SCPM-2-2 was 1.75 GPa and 2.24 GPa, respectively. The hardness of the inner side of the ITZ at SCPM-2-1 was significantly lower than that of the outer side, which was probably due to the gap between the cement paste and the DCL. The average hardness of ITZ at SCPM-2-3, SCPM-2-4 and SCPM-2-5 was only 0.89 GPa, 0.89 GPa and 0.44 GPa, respectively, which can be explained by the previous discussion on the distribution of pores and particles. In contrast, the average hardness of the matrix at SCPM-2-1, SCPM-2-2, SCPM-2-3, SCPM-2-4 and SCPM-2-5 was 1.77 GPa, 2.23 GPa, 0.96 GPa, 1.82 GPa and 1.17 GPa, respectively.

3.5. Elements distribution

The EDS hypermaps of SCPM-1 and SCPM-2 within $50 \times 34 \mu\text{m}$ rectangle areas near the DCL surface are shown in Figs. 17 and 18 respectively. If the observation area is attached to the DCL surface, the test results will inevitably interfere with the constituents in the DCLs because of the rough DCL surface [46]. Therefore, there was a gap of about 20 μm between the DCLs and the observation areas. The rectangle observing area was artificially set to avoid large cracks, pores, and unreacted particles. It has to be admitted that for some locations, the observation area may include part of the ITZ and matrix, while for other locations, only the matrix exists in the observation area. Previous studies have confirmed that there is no significant difference in the chemical

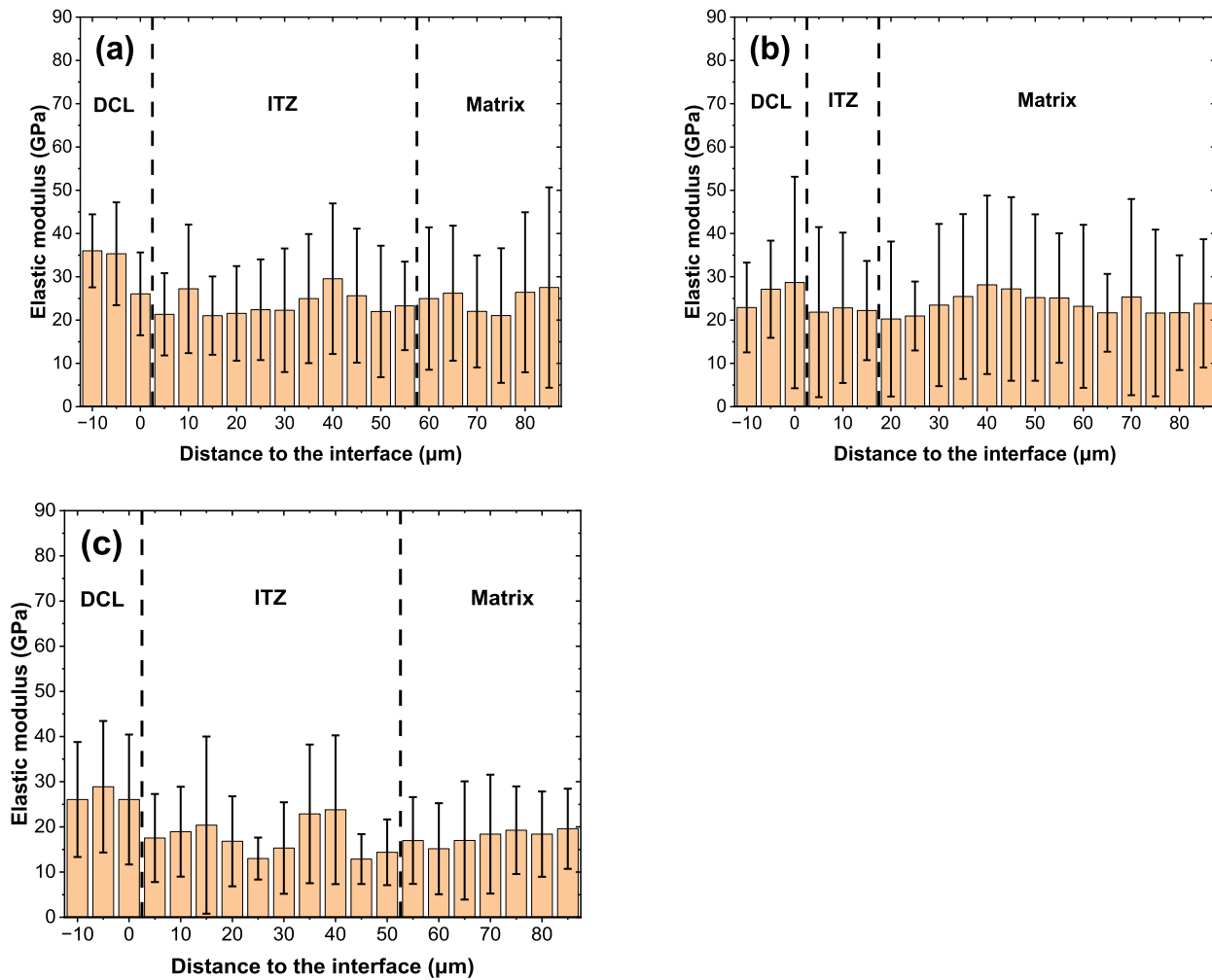


Fig. 13. Elastic modulus of SCPM-1 around DCL: (a) SCPM-1-1; (b) SCPM-1-2; (c) SCPM-1-3.

composition between ITZ and matrix because they are made from the same raw materials [26]. Therefore, the operation here is unavoidable and acceptable.

As shown in Fig. 17(a)–(c), each location of SCPM-1 was rich in Ca and Si, which were the main elements of C-S-H gel and portlandite. In addition, SCPM-1 contains RP with a high content of Na₂O, K₂O and Al₂O₃ (see Table 3). As a result, some concentrated areas of Na, K and Al elements can be observed in hypermaps. SCPM-2 contains 25 % fly ash with an obviously higher proportion of Al and Si elements than cement. Therefore, more Al and Si circular concentration areas can be observed in Fig. 18(a)–(e). However, the differences in the weight fractions of Na₂O and K₂O between fly ash and RP were only 0.52 wt% and 0.01 wt %, respectively according to Table 3. Therefore, there was no significant difference between the Na and K elements hypermaps of SCPM-2 and SCPM-1.

Most phases in cement paste can be segmented according to Al/Ca vs. Si/Ca ratio under an ideal condition [47]. However, cementitious materials are generally complicated and heterogeneous, especially for RLC prepared by the unique procedure. It is impossible to clearly divide scatter plots into a series of points or clusters corresponding to specific phases. Figs. 19 and 20 show the quantitative results of the above hypermaps (Figs. 17 and 18). The coloured circles represent relatively pure phases at the microvolume level [33,34]. It can be seen that most of the data points belong to the mixed phase of C-S-H and CH, clinkers or crystals.

As shown in Fig. 19(a) and (b), the point clusters corresponding to Ferrite phase, Aluminate phase, pozzolanic materials and C-S-H with

higher Al/Ca ratio at SCPM-1-2 were denser than those at SCPM-1-1, which is attributed to the presence of more RS/RP sediments at SCPM-1-2. In comparison, SCPM-1-3 contained almost no other pure phases and pozzolanic materials except C-S-H gel and several C-S-H intermixed phases. SCPM-1 achieved self-compacting ability due to its excessively high water-cement ratio (0.5). However, in this case, the distribution of the constituents in the mortar was extremely unstable. Most of the particles, such as unhydrated clinkers, RS and RP, stayed at SCPM-1-1 and SCPM-1-2. Combined with the analysis in Section 3.2, SCPM-1-3 was mainly constituted with C-S-H gel, pores and cracks.

Benefiting from the function of superplasticizer and fly ash, the scatter plots of SCPM-2 shown in Fig. 20 are more stabilized than those of SCPM-1, which is consistent with the conclusion on the equivalent diameter distribution of pores and cracks obtained in Section 3.3. By comparing the locations #1, #2 and #3 of SCPM-1 and SCPM-2, it can be found that the line corresponding to the pozzolanic materials in SCPM-2 was more obvious because SCPM-2 contains 25 % fly ash. Although SCPM-2 had better stability than SCPM-1, the content of pozzolanic materials in SCPM-2-1 and SCPM-2-2 was higher than that in SCPM-2-3 due to the sedimentation. This result also led to differences in C-S-H and Portlandite clusters. There was a cluster extending into the pure Portlandite area at SCPM-2-3, SCPM-2-4 and SCPM-2-5, while pure Portlandite was almost non-existent at SCPM-2-1 and SCPM-2-2 because the pozzolanic materials stayed at SCPM-2-1 and SCPM-2-2 consumed Ca(OH)₂ and generated more C-S-H with higher Si/Ca ratio. In addition, it is worth noting that the Al/Ca and Si/Ca ratios of C-S-H at SCPM-2-1, SCPM-2-2 and SCPM-2-4 were around 0.2 and 0.9, respectively, while

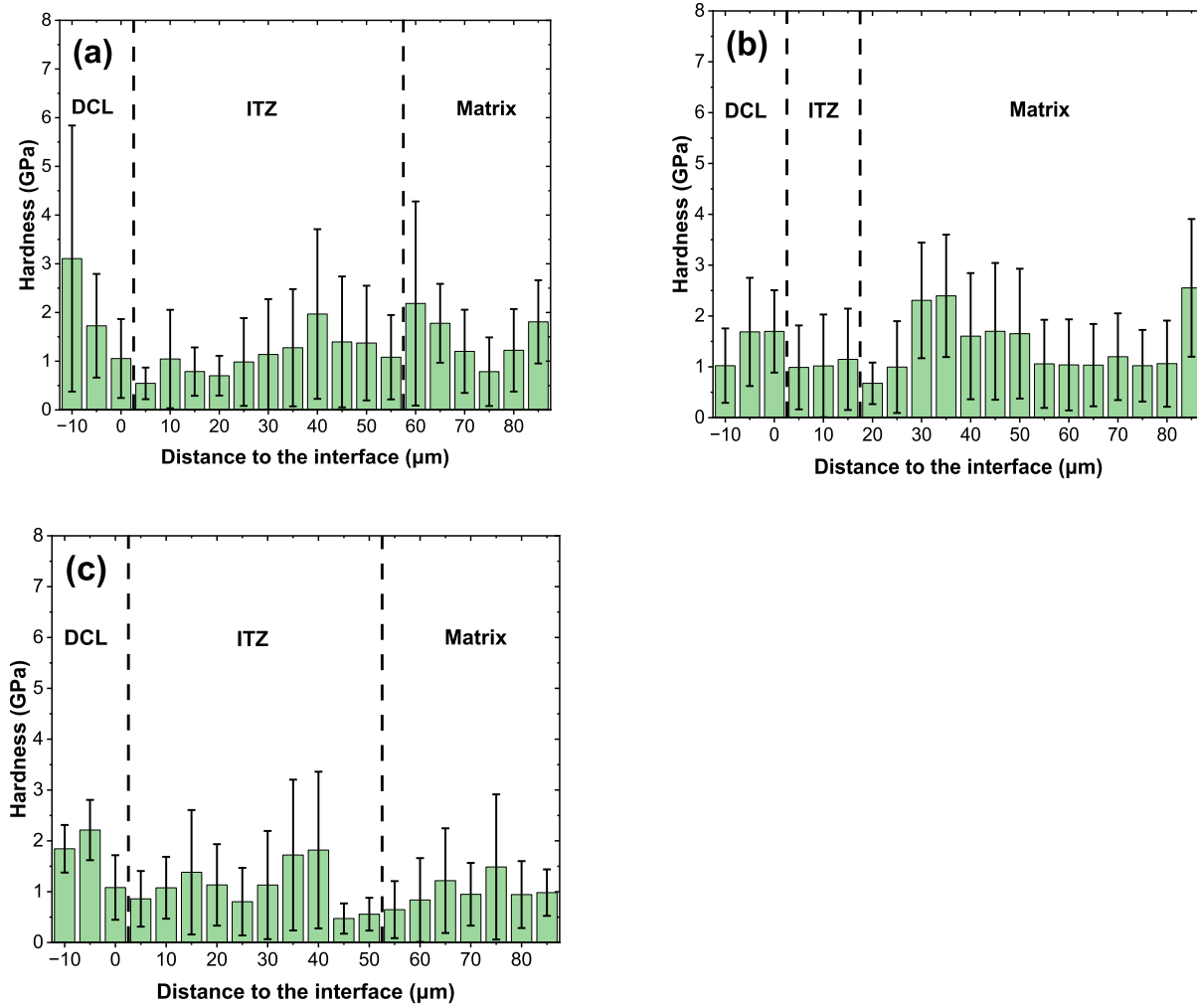


Fig. 14. Hardness of SCPM-1 around DCL: (a) SCPM-1-1; (b) SCPM-1-2; (c) SCPM-1-3.

the corresponding ratios of C-S-H at SCPM-2-3 and SCPM-2-5 were only around 0.15 and 0.5. This indicates that most of the C-S-H gel at SCPM-2-3 and SCPM-2-5 were loose and porous outer C-S-H with low Si/Ca ratio [34], which is probably due to the high distances between cement grains in these two locations. This also proves that SCPM-2-3 and SCPM-2-5 were the vulnerable regions in the RLP prepared by SCPM-2, which is consistent with nanoindentation test results in Section 3.4. The scatter plot of SCPM-2-4 was not as concentrated as the other four regions, which means that there were more mixed phases of C-S-H and Ferrite, Aluminite and pozzolanic materials. The complicated morphological conditions of the oblique bottom side of the DCL with the surrounding environment and the vortex shedding of SCPM-2 probably together created this result.

4. Discussions

4.1. Properties of ITZs around DCLs

The relative contents of the main phases in the ITZ and matrix around DCL can be roughly inferred by analysing the corresponding cement paste samples at the micro-level. Due to the slightly poor filling capacity of SCPM-1, no qualified samples could be prepared from the bottom side and oblique bottom side of DCL. In RLC fabricated by SCPM-1, only the phase information within the ITZ and matrix located on the top, oblique top and lateral sides of the DCL was obtained. Based on the test results, the constituent relative quantity proportion distribution of

the two groups of samples in this study can be summarized in Fig. 21.

In RLC, unreacted particles were mostly concentrated on the top side and oblique top sides of DCL due to sedimentation effect. As can be seen from Fig. 21, the ITZ on the lateral side of the DCL had a higher proportion of small-sized pores and cracks than the other two regions. Many previous studies on the concrete pore structure pointed out that large-sized pores transformed into small-sized pores in the modification process of concrete microstructure [48]. Therefore, in the test results, the number of small-sized pores increased, and the number of large-sized pores decreased in the concrete sample after the microstructure modification. This seems inconsistent with the results obtained in this study. In fact, the casting method of RLC is significantly different from that of traditional concrete or RAC. When producing RLC specimens, DCLs were packed in a mould and then the gaps between DCLs were filled depending on the high fluidity of SCPM. The mixing and vibration processes were missed in this procedure. Therefore, there may be more oversized pores in the cement paste around the DCL than in ordinary concrete. These pores and cracks are so large that grains and additionally generated C-S-H gel are not sufficient to fill them into small pores below 0.5 μm, whereas the small-sized pores originally existing in the cement paste can be filled more effectively. As a result, the microstructure of ITZ located on the top and oblique top sides of the DCL was denser and had a lower proportion of small-sized pores and cracks with 0.2–0.3 μm. This situation was alleviated in the matrix because the wall effect from the DCL can be ignored in this region. The porosity within the matrix of RLC fabricated by SCPM-1 was generally lower than that of

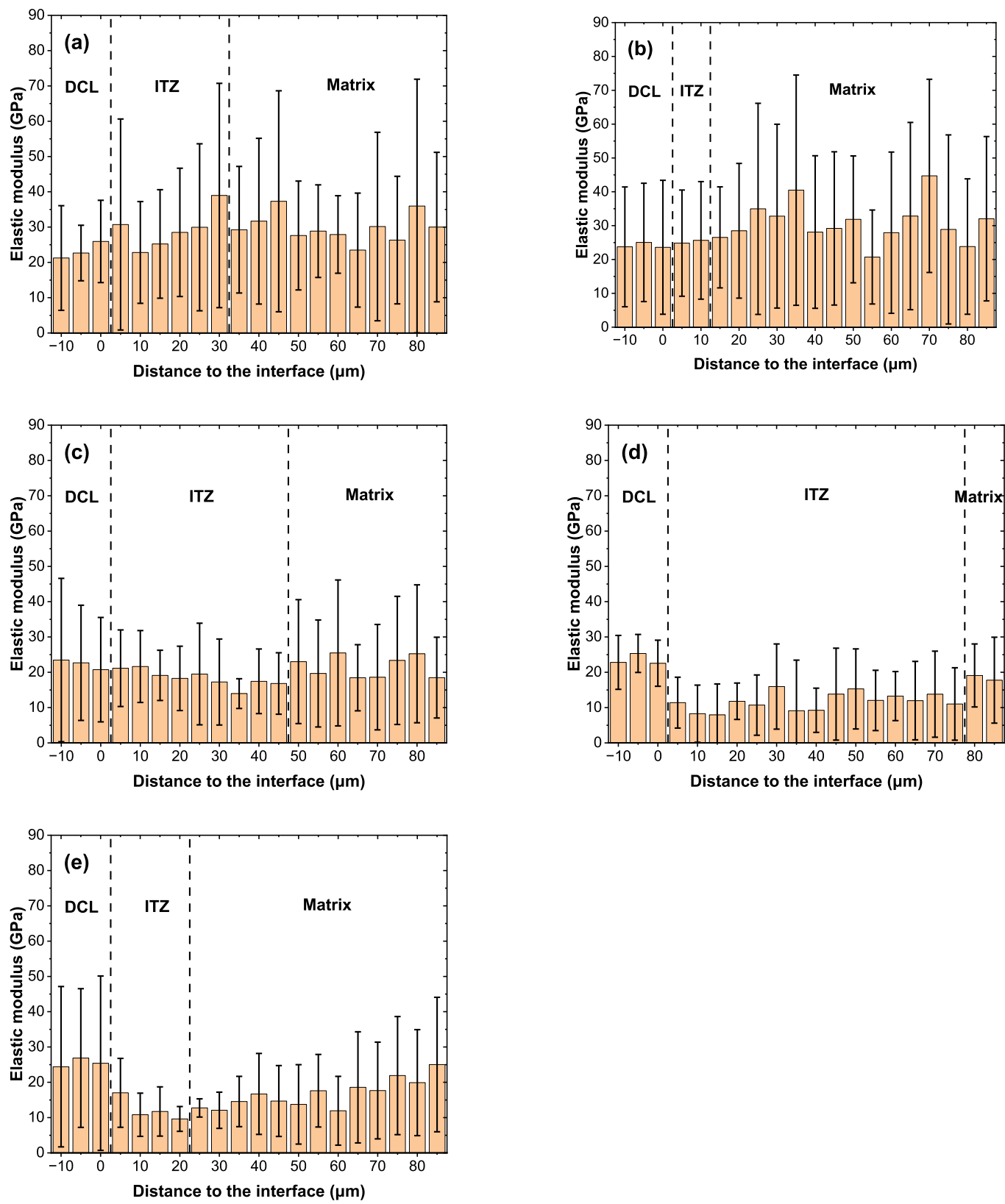


Fig. 15. Elastic modulus of SCPM-2 around DCL: (a) SCPM-2-1; (b) SCPM-2-2; (c) SCPM-2-3; (d) SCPM-2-4; (e) SCPM-2-5.

ITZ, and the matrix possessed a higher proportion of C-S-H gel. However, due to sedimentation, the grains in the top and oblique top sides matrix were less than those in corresponding ITZs, and this situation was reversed on the lateral side of DCL. The filling performance of SCPM-2

was better than that of SCPM-1, so there was no obvious difference in the relative proportions of phases around the DCL. For the bottom side and oblique bottom side of DCL, the bonding strength of these two areas was weaker than that of the top side and oblique top side due to the

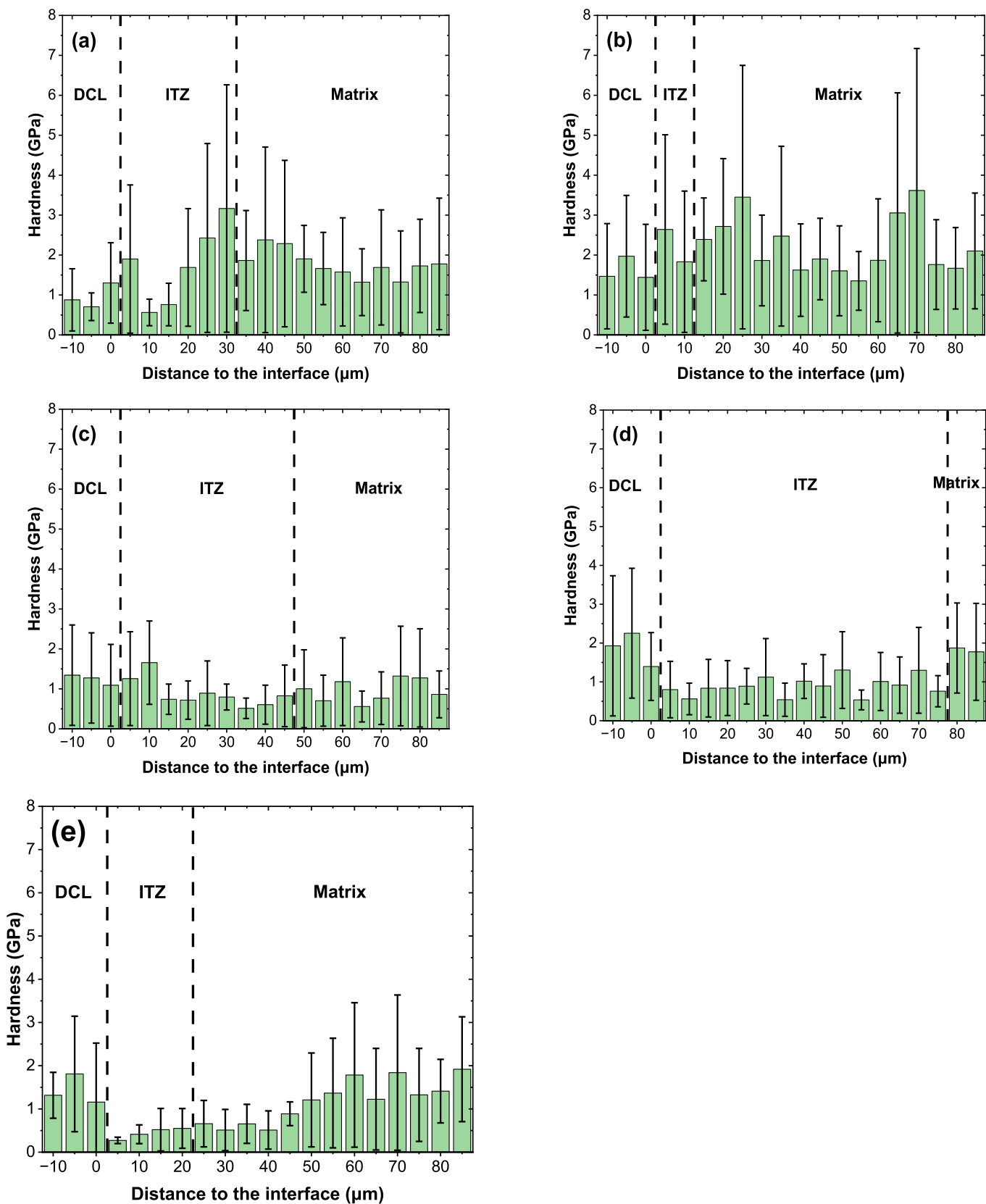


Fig. 16. Hardness of SCPM-2 around DCL: (a) SCPM-2-1; (b) SCPM-2-2; (c) SCPM-2-3; (d) SCPM-2-4; (e) SCPM-2-5.

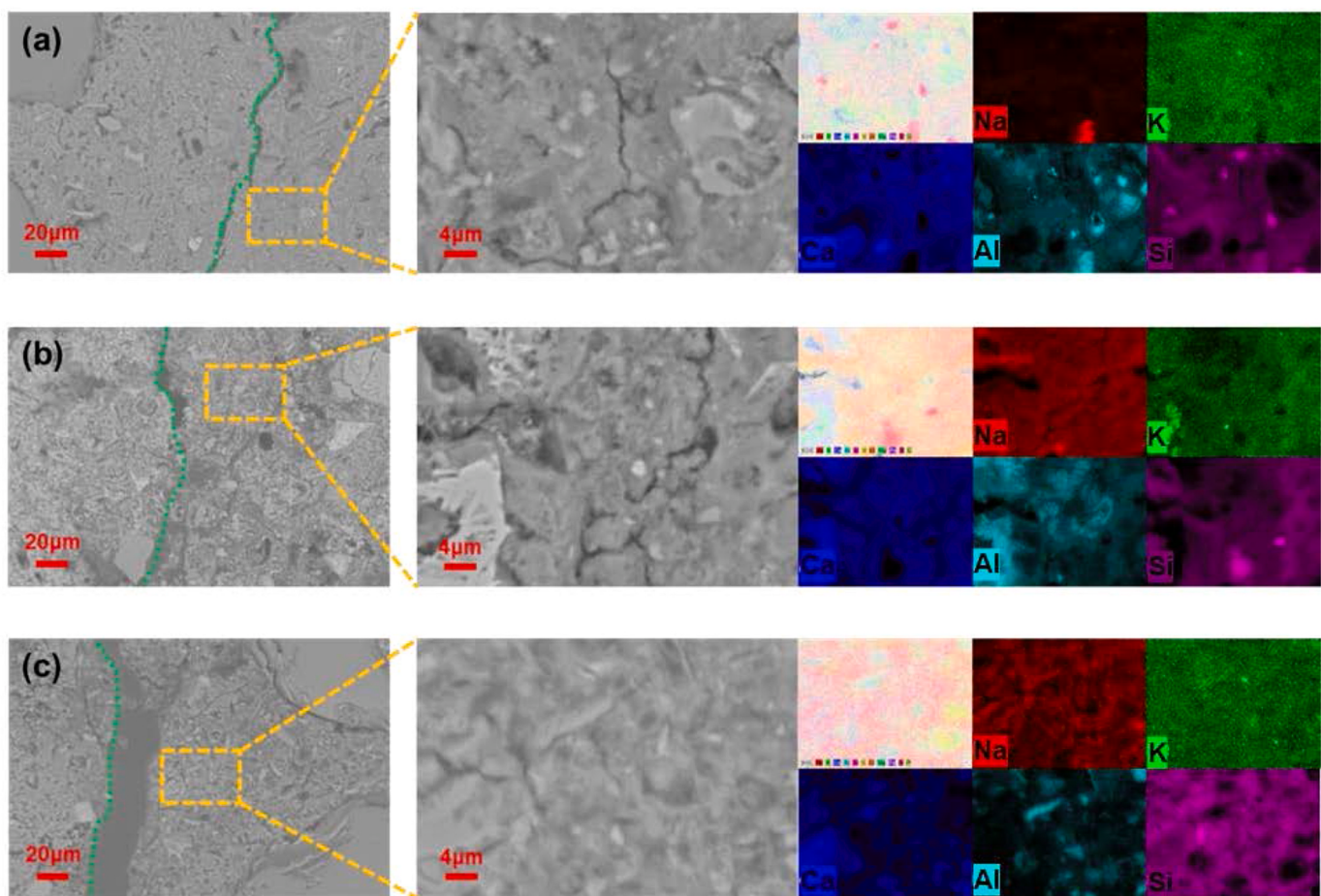


Fig. 17. BSE-EDS hypermaps of SCPM-1 matrix adjacent to DCL: (a) SCPM-1-1; (b) SCPM-1-2; (c) SCPM-1-3.

relative relationship between the yield stress and shear stress generated by the gravity of SCPM-2.

In general, there is an obvious heterogeneity between the cement paste in different regions around the DCL. This heterogeneity is mainly reflected in pore size and grain distribution. However, the fluidity of SCPM, the reaction of supplementary cementitious materials and the surrounding morphology will have different degrees of influence on ITZ and matrix. The test results are inevitably variable. Moreover, this study ignores the impact of the DCL being located in the upper or lower layer of the mould. Therefore, discussing RLC heterogeneity is a very complicated and hard work. This study designed two types of SCPM, among which SCPM-1 did not contain any special additives. To ensure ideal flowability and avoid serious bleeding of SCPM, the water-cement ratio of SCPM-1 was determined to 0.5 after repeated attempts. Although SCPM-1 seemingly filled the gap between the DCLs from the surface of specimens, we were not able to successfully produce ITZ samples located on the bottom and oblique bottom sides of the DCL. There were also obvious differences in the performance of cement paste located in the rest three regions. Among them, the bonding performance of cement paste on the top side and the oblique top side was better than that on the lateral side. In comparison, SCPM-2 performed more consistently around the DCL. However, it can still be seen that the bonding performance of the cement paste located on the top side and the oblique top side was better than that of the other three regions.

4.2. Nano- and micro-characterization techniques on ITZs

Cement-based materials contain C-S-H gel, CH, clinkers, pores, ettringite etc., which are typical inhomogeneous materials. The study of

ITZ microscopic properties is more difficult because in addition to mixture proportion, ITZ performance is also affected by aggregate surface morphology. Some scholars proposed the theory of model aggregate concrete (MAC) [26,27]. In their research, aggregate was processed into a cubic block to quickly identify the performance of ITZ. However, this method ignores some important features, such as the accumulation of free water and grinds caused by holes and edges on the aggregate surface. This will undoubtedly overestimate the cohesion strength of ITZs. Therefore, the application of model aggregate concrete in ITZ research is still controversial. On the other hand, existing nano/microscopic characterization techniques, including SEM, nanoindentation, modulus mapping and PeakForce QNM, can only provide local information of the material. This is unreliable for cement paste and ITZ with strong inhomogeneity. As a result, we prepared multiple samples (three samples for SCPM-1 and five samples for SCPM-2) around DCLs. BSE-image analysis, nanoindentation and BSE-EDS hypermap analysis techniques were combined to discuss the microscopic properties of the ITZ in the RLC as comprehensively as possible. However, the limitations of existing nano/microscopic characterization techniques still cannot be completely avoided. Although blindly increasing the workload can improve the accuracy of the test results, it will also bring unbearable financial and time costs. We have made efforts to improve the accuracy of the test and believe that this study can guide in-depth exploration of the mechanical properties and durability of RLC. At present, it is still challenging to fully and accurately understand the microstructure and micromechanical properties of cementitious materials and ITZ. In the future, more testing instruments and technical strategies can be developed for quantitative characterization of cement-based materials.

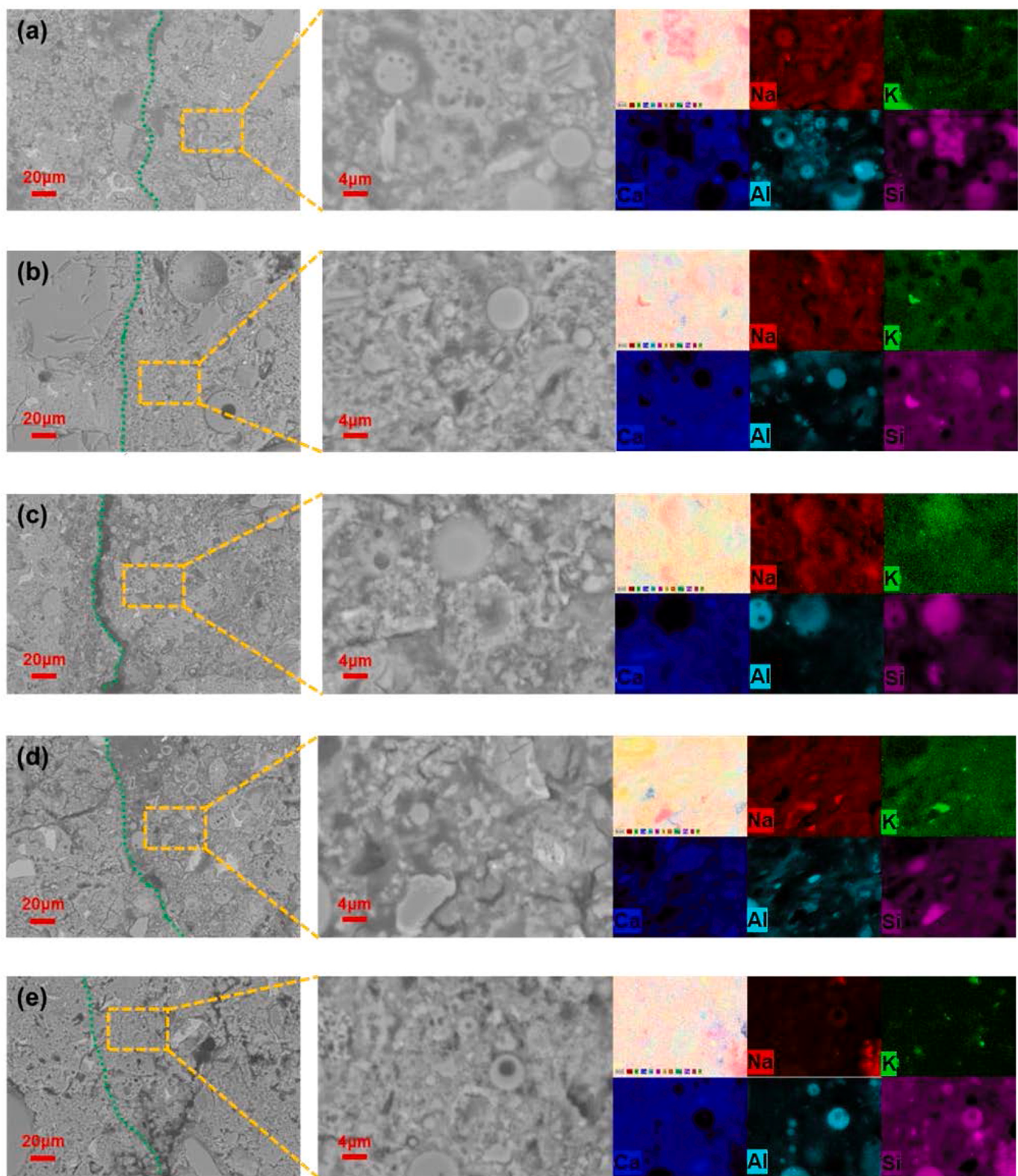


Fig. 18. BSE-EDS hypermaps of SCPM-2 matrix adjacent to DCL: (a) SCPM-2-1; (b) SCPM-2-2; (c) SCPM-2-3; (d) SCPM-2-4; (e) SCPM-2-5.

5. Conclusions

Two types of SCPM were designed to prepare RLC, and samples around DCLs from top side to bottom side were fabricated to investigate the heterogeneity of ITZs and adjacent paste matrix. The BSE-image analysis, nanoindentation and EDS hypermap quantitative analysis

techniques supported each other to make a comprehensive assessment of the ITZ performance in RLC. The main conclusions can be drawn up as follows:

- (1) Two types of SCPM with cement and RP/RS blends as the main raw materials were designed in this study. From an external

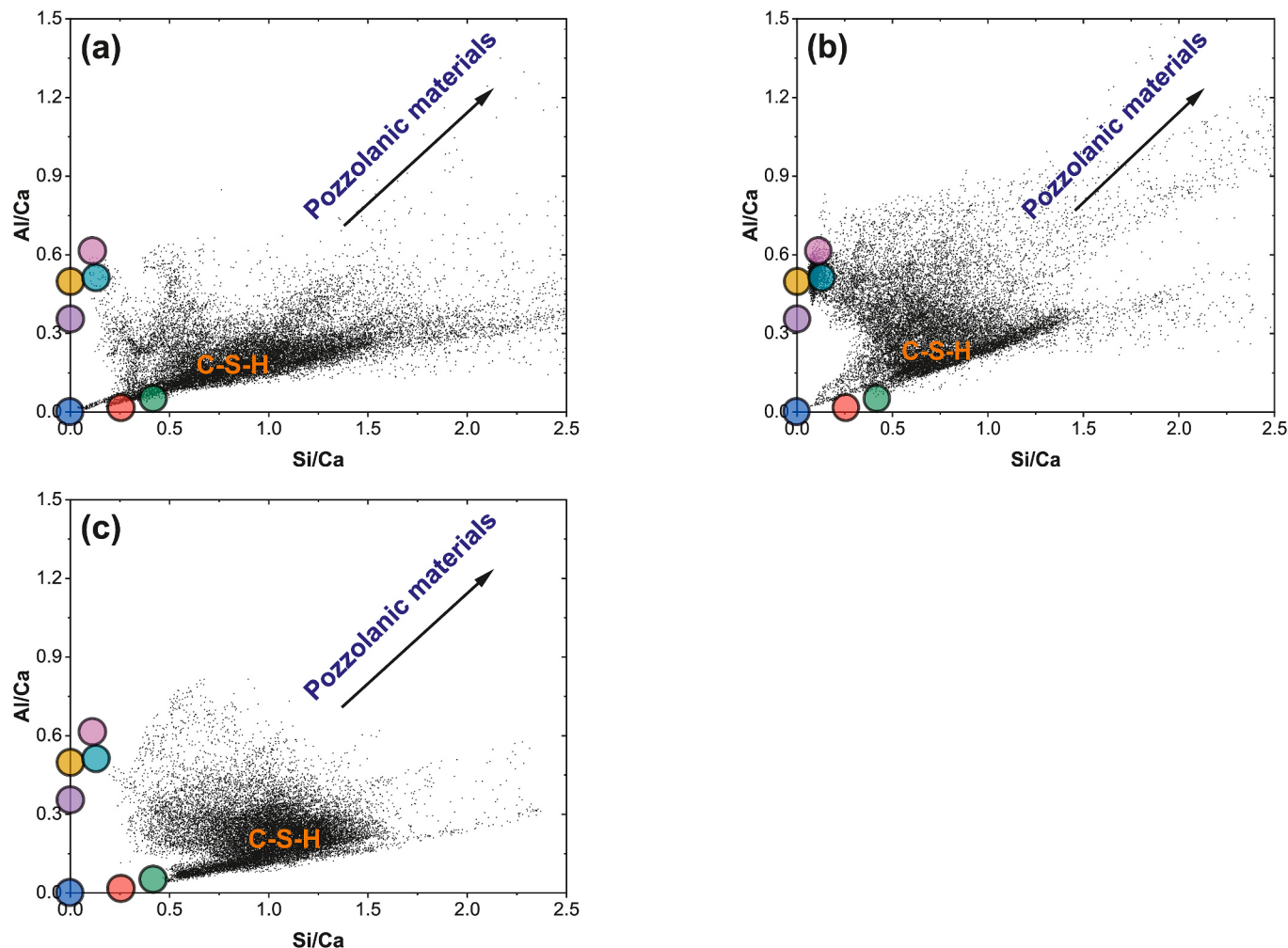


Fig. 19. EDS hypermaps quantitative analysis results of SCPM-1 at different locations: (a) SCPM-1-1; (b) SCPM-1-2; (c) SCPM-1-3.

Note: ● Portlandite ● Alite ● Belite ● Aft ● AFm ● Ferrite ● Aluminate.

observation, both types of SCPM can successfully fill gaps between DCLs. Cubic RLC specimens can achieve more than 30 MPa of compressive strength at 28 days. However, SCPM-1 produced by an excessively high water-cement ratio cannot achieve a relatively strong bonding strength at the bottom and oblique bottom sides of DCLs. Additives such as superplasticizer and fly ash are necessary in preparing RLC.

- (2) Fly ash and superplasticizer help to make the distribution of pores and particles in ITZ and matrix around DCLs more uniform. The CoD_U of unreacted particles in SCPM-1-3 without fly ash and superplasticizer was stable at around 6.0, while the CoD_U of SCPM-2 with fly ash and superplasticizer was always below 1.0 in all locations. Nevertheless, due to the special preparing procedure of RLC, the ITZs of RLC were generally wider than those of ordinary concrete, especially for the ITZ widths of SCPM-1-1 (58 μm), SCPM-1-3 (53 μm) and SCPM-2-4 (78 μm), which were beyond the ITZ width range of NAC.
- (3) The #1, #2 and #3 locations of SCPM-1 contained dense small pores with an average equivalent diameter of 0.2–0.3 μm , while the pore diameters in each region of SCPM-2 were more evenly distributed in a wide range because the RP (high proportion of CaO) and fly ash (high proportion of effective SiO₂) in SCPM-2

can more effectively reduce the relative proportion of small-sized pores through secondary hydration and pozzolanic reaction, respectively. Similar phenomena also exist in the matrix. However, due to the poor wall effect, the heterogeneity of the matrix is weakened compared with the adjacent ITZ.

- (4) Due to the sedimentation effect of unreacted particles, the micromechanical properties of ITZ at SCPM-1-1 and SCPM-1-2 were higher than SCPM-1-3, which means cement paste at SCPM-1-3 cannot form a strong bond with the DCL. The micromechanical properties of SCPM-2 around the DCL were higher than those of the corresponding regions of SCPM-1. The cement paste at SCPM-2-4 and SCPM-2-5 had the worst cohesion strength.
- (5) The high water-cement ratio of SCPM-1 led to serious particle sedimentation. The distribution of constituents in the three locations was obviously different. In comparison, the RLC prepared by SCPM-2 had better consistency around the DCL. However, it can still be seen that the particles were mainly concentrated on the top and oblique top sides of the DCL. Combined with the gravity effect of SCPM, the bonding performance of the cement paste at the top and oblique top side of the DCL was better than that of the other three locations.

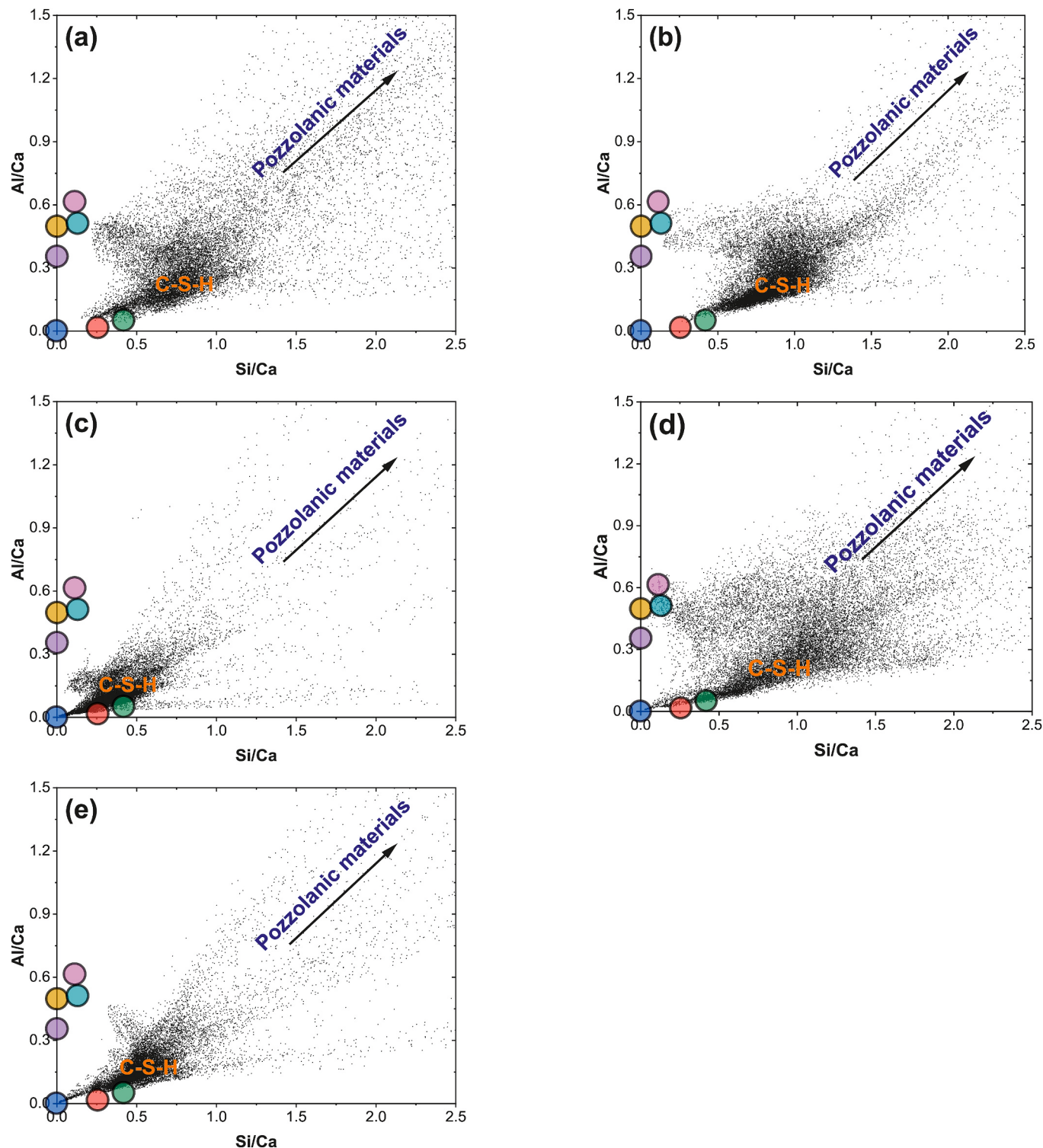


Fig. 20. EDS hypermaps quantitative analysis results of SCPM-2 at different locations: (a) SCPM-2-1; (b) SCPM-2-2; (c) SCPM-2-3; (d) SCPM-2-4; (e) SCPM-2-5.
Note: ● Portlandite ● Alite ● Belite ● AFt ● AFm ● Ferrite ● Aluminate.

- (6) Existing nano/microscopic characterization techniques on materials can only provide local microstructure or micromechanical properties information. For concrete materials with high inhomogeneity, it is difficult to obtain accurate and reliable

conclusions through limited test workload. Although simplification methods such as MAC technique alleviate the influence of aggregate surface morphology on ITZs performance, they also over-idealize the concrete inner structure. It remains challenging

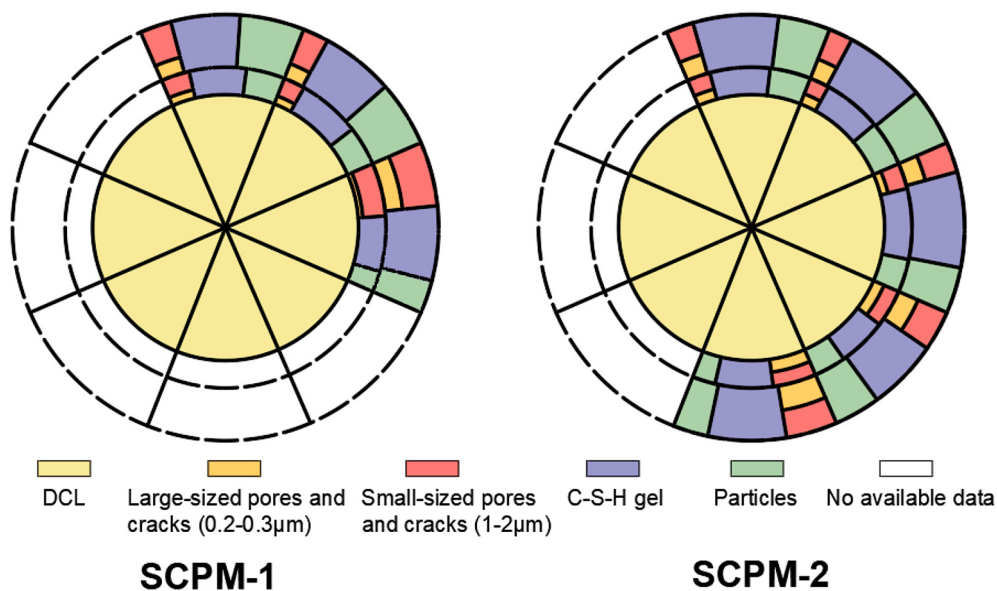


Fig. 21. Schematic diagram of constituent relative proportion distribution around DCL.

to comprehensively understand cementitious materials and ITZs using existing technologies while controlling testing costs. In the future, more efficient line scan, mapping scan and volume scan techniques can be developed for concrete materials, such as nanoscratch technique and X-ray computed tomography which can obtain massive data in a short time.

CRediT authorship contribution statement

Hanbing Zhao: Writing – review & editing, Writing – original draft, Validation, Methodology, Investigation, Formal analysis, Conceptualization. **Yixiang Gan:** Writing – review & editing, Writing – original draft, Validation, Supervision, Resources. **Fulin Qu:** Writing – review & editing, Writing – original draft, Validation. **Zhuo Tang:** Writing – review & editing, Writing – original draft. **Shuhua Peng:** Writing – review & editing, Writing – original draft, Supervision, Resources. **Yangqiao Chen:** Writing – review & editing, Writing – original draft. **Wengui Li:** Writing – review & editing, Writing – original draft, Validation, Supervision, Resources, Conceptualization.

Declaration of competing interest

The authors declare that they have no known competing financial interests or personal relationships that could have appeared to influence the work reported in this paper.

Acknowledgements

The authors would like to acknowledge the support from the Australian Research Council (ARC), Australia (FT220100177, LP230100288, DP220101051, DP220100036 and IH200100010).

Data availability

Data will be made available on request.

References

- [1] J. Yan, B. Wu, Mechanical behavior of recycled lump concrete containing mixed demolished concrete lumps with different sizes or/and shapes, *J. Build. Eng.* 86 (2024) 108753.
- [2] S. Jian, B. Wu, N. Hu, Environmental impacts of three waste concrete recycling strategies for prefabricated components through comparative life cycle assessment, *J. Clean. Prod.* 328 (2021) 129463.
- [3] S. Jian, B. Wu, Compressive behavior of compound concrete containing demolished concrete lumps and recycled aggregate concrete, *Constr. Build. Mater.* 272 (2021) 121624.
- [4] B. Wu, Z. Wang, Z. Chen, Shrinkage behavior of recycled lump/aggregate concrete containing recycled sand from weathered residual soil of granite, *Constr. Build. Mater.* 394 (2023) 132146.
- [5] S. He, Z. Zhu, M. Lv, H. Wang, Experimental study on the creep behaviour of rock-filled concrete and self-compacting concrete, *Constr. Build. Mater.* 186 (2018) 53–61.
- [6] Y. Wang, F. Jin, Y. Xie, Experimental study on effects of casting procedures on compressive strength, water permeability, and interfacial transition zone porosity of rock-filled concrete, *J. Mater. Civ. Eng.* 28 (8) (2016) 04016055.
- [7] X. An, Q. Wu, F. Jin, M. Huang, H. Zhou, C. Chen, C. Liu, Rock-filled concrete, the new norm of SCC in hydraulic engineering in China, *Cement Concr. Compos.* 54 (2014) 89–99.
- [8] T. Zhang, B. Wu, Compressive behavior and water permeability of recycled lump-aggregate concrete with recycled sand from weathered residual soil of granite, *Constr. Build. Mater.* 419 (2024) 135487.
- [9] B. Wu, X. Yang, J.J. Zhang, G.M. Chen, X.Y. Zhao, Recycled lump concrete-filled FRP tubular columns: axial compressive behavior and size effects, *Constr. Build. Mater.* 352 (2022) 129000.
- [10] J. Yan, B. Wu, Flexural behavior of recycled lump concrete made with demolished concrete lumps of different sizes and shapes, *Constr. Build. Mater.* 307 (2021) 124940.
- [11] B. Wu, J. Zang, Effect of embedded steel stirrups on fire behavior of square steel tubular columns filled with recycled lump concrete, *Eng. Struct.* 211 (2020) 110446.
- [12] L. Lin, B. Wu, Water permeability behavior of recycled lump/aggregate concrete, *Constr. Build. Mater.* 323 (2022) 126508.
- [13] J. Liu, K. Ma, J. Shen, J. Zhu, G. Long, Y. Xie, B. Liu, Influence of recycled concrete aggregate enhancement methods on the change of microstructure of ITZs in recycled aggregate concrete, *Constr. Build. Mater.* 371 (2023) 130772.
- [14] X. Gao, Q. Liu, Y. Cai, L. Tong, Z. Peng, Q. Xiong, G.D. Schutter, A new model for investigating the formation of interfacial transition zone in cement-based materials, *Cement Concr. Res.* 187 (2025) 107675.
- [15] H. Zhang, X. Xu, W. Liu, B. Zhao, Q. Wang, Influence of the moisture states of aggregate recycled from waste concrete on the performance of the prepared recycled aggregate concrete (RAC) – a review, *Constr. Build. Mater.* 326 (2022) 126891.
- [16] M.M. Thakur, N.A. Henningsson, J. Engqvist, P.-O. Autran, J.P. Wright, R.C. Hurley, On mesoscale modeling of concrete: role of heterogeneities on local stresses, strains, and representative volume element, *Cement Concr. Res.* 16 (2023) 107031.
- [17] Y. Xie, D.J. Corr, F. Jin, H. Zhou, S.P. Shah, Experimental study of the interfacial transition zone (ITZ) of model rock-filled concrete (RFC), *Cement Concr. Compos.* 55 (2015) 223–231.
- [18] Y. Xie, D.J. Corr, M. Chauache, F. Jin, S.P. Shah, Experimental study offilling capacity of self-compacting concrete and its influence on the properties of rock-filled concrete, *Cement Concr. Res.* 56 (2014) 121–128.
- [19] Z. Luo, W. Li, K. Wang, S.P. Shah, D. Sheng, Nano/micromechanical characterisation and image analysis on the properties and heterogeneity of ITZs in geopolymer concrete, *Cement Concr. Res.* 152 (2022) 106677.

- [20] Y. Guo, F. Qu, R. Tiwari, D.Y. Yoo, K. Wang, Y. Wang, Development of self-sensing asphalt cementitious composites using conductive carbon fibre and recycled copper tailing, *Constr. Build. Mater.* 474 (2025) 140965.
- [21] Y. Guo, F. Qu, Advancing circular economy and construction sustainability: transforming mine tailings into high-value cementitious and alkali-activated concrete, *npj Mater. Sustain* 3 (1) (2025) 8.
- [22] F. Qu, Y. Zhang, M. Li, W. Dong, W. Li, Resource recycling of industrial waste phosphogypsum in cementitious materials: Pretreatment, properties, and applications, *J. Environ. Manag.* 376 (2025) 124291.
- [23] A.K.H. Kwan, W.W.S. Fung, Effects of SP on flowability and cohesiveness of cement-sand mortar, *Constr. Build. Mater.* 48 (2013) 1050–1057.
- [24] S.-D. Hwang, K.H. Khayat, R. Morin, Specifications and testing of self-consolidating mortar designated for annular space grouting, *Can. J. Civ. Eng.* 38 (4) (2011) 422–432.
- [25] Z. Zhu, J.L. Provis, H. Chen, Quantification of the influences of aggregate shape and sampling method on the overestimation of ITZ thickness in cementitious materials, *Powder Technol.* 326 (2018) 168–180.
- [26] H. Zhao, W. Li, Y. Gan, K. Wang, Z. Luo, Nano/microcharacterization and image analysis on bonding behaviour of ITZs in recycled concrete enhanced with waste glass powder, *Constr. Build. Mater.* 392 (2023) 131904.
- [27] Z. Luo, W. Li, K. Wang, A. Castel, S.P. Shah, Comparison on the properties of ITZs in fly ash-based geopolymers and Portland cement concretes with equivalent flowability, *Cement Concr. Res.* 143 (2021) 106392.
- [28] Y. Li, H. Zhao, Y. Hu, F. Qu, D. Zhu, K. Wang, W. Li, Effect of pore water pressure on mechanical performance of recycled aggregate concrete under triaxial compression, *Cement Concr. Compos.* 146 (2024) 105402.
- [29] Z. Zhang, J. Qin, Z. Ma, X. Pang, Y. Zhou, Comparison of three different deconvolution methods for analyzing nanoindentation test data of hydrated cement paste, *Cement Concr. Compos.* 138 (2023) 104990.
- [30] Z. Luo, W. Li, Y. Gan, K. Mendu, S.P. Shah, Applying grid nanoindentation and maximum likelihood estimation for N-A-S-H gel in geopolymers paste: investigation and discussion, *Cement Concr. Res.* 135 (2020) 106112.
- [31] H.S. Wong, M.K. Head, N.R. Buenfeld, Pore segmentation of cement-based materials from backscattered electron images, *Cement Concr. Res.* 36 (2006) 1083–1090.
- [32] H. Zhao, Y. Hu, Y. Li, K. Wang, F. Dehn, W. Li, Triaxial compressive performance of recycled aggregate/glass sand concrete: experimental study and mechanism analysis, *J. Clean. Prod.* 442 (2024) 141006.
- [33] F. Georget, W. Wilson, K.L. Scrivener, edxia: microstructure characterisation from quantified SEM-EDS hypermaps, *Cement Concr. Res.* 141 (2021) 106327.
- [34] P. Li, W. Li, K. Wang, H. Zhao, S.P. Shah, Hydration and microstructure of cement paste mixed with seawater – an advanced investigation by SEM-EDS method, *Constr. Build. Mater.* 392 (2023) 131925.
- [35] A. Aghaeipour, M. Madhkhani, Mechanical properties and durability of roller compacted concrete pavement (RCCP)-a review, *Road Mater. Pavement Des.* 21 (7) (2020) 1775–1798.
- [36] B. Zhan, D. Xuan, C.S. Poon, K.L. Scrivener, Characterization of interfacial transition zone in concrete prepared with carbonated modeled recycled concrete aggregates, *Cement Concr. Res.* 136 (2020) 106175.
- [37] X. Gao, Z. Peng, L. Tong, Y. Cai, J. Xiao, X. Geng, Q. Liu, Effect of global aggregate distribution on interfacial transition zones in cement-based materials: an analytical-numerical study, *Constr. Build. Mater.* 458 (2025) 138278.
- [38] Q. Wu, X. An, Development of a mix design method for SCC based on the rheological characteristics of paste, *Constr. Build. Mater.* 53 (2014) 642–651.
- [39] A.M. Zeyad, A. Almaliki, Influence of mixing time and superplasticizer dosage on self-consolidating concrete properties, *J. Mater. Res. Technol.* 9 (3) (2020) 6101–6115.
- [40] G. Fang, M. Zhang, The evolution of interfacial transition zone in alkali-activated fly ash-slag concrete, *Cement Concr. Res.* 129 (2020) 105963.
- [41] P.R. Rangaraju, J. Olek, S. Diamond, An investigation into the influence of inter-aggregate spacing and the extent of the ITZ on properties of Portland cement concretes, *Cement Concr. Res.* 40 (11) (2010) 1601–1608.
- [42] M. Kuroda, T. Watanabe, N. Terashi, Increase of bond strength at interfacial transition zone by the use of fly ash, *Cement Concr. Res.* 30 (2) (2000) 253–258.
- [43] S. Hou, R. Hu, L. Xu, Y. Zhang, Z. Ma, Understanding the chloride migration in recycled powder concrete: effects of recycled powder type, replacement rate and substitution pattern, *Constr. Build. Mater.* 436 (2024) 136825.
- [44] W. Li, J. Xiao, Z. Sun, S. Kawashima, S.P. Shah, Interfacial transition zones in recycled aggregate concrete with different mixing approaches, *Constr. Build. Mater.* 35 (2012) 1045–1055.
- [45] J. Xiao, W. Li, Z. Sun, D.A. Lange, S.P. Shah, Properties of interfacial transition zones in recycled aggregate concrete tested by nanoindentation, *Cement Concr. Compos.* 37 (2013) 276–292.
- [46] F. Georget, C. Benier, W. Wilson, K.L. Scrivener, Chloride sorption by C-S-H quantified by SEM-EDX image analysis, *Cement Concr. Res.* 152 (2022) 106656.
- [47] J.W. Bullard, H.M. Jennings, R.A. Livingston, A. Nonat, G.W. Scherer, J. Schweitzer, K.L. Scrivener, J.J. Thomas, Mechanisms of cement hydration, *Cement Concr. Res.* 41 (2011) 1208–1223.
- [48] A.A. Hamami, P. Turcay, A. Aït-Mokhtar, Influence of mix proportions on microstructure and gas permeability of cement pastes and mortars, *Cement Concr. Res.* 42 (2012) 490–498.